



# Ionic liquid-employed synthesis of $\text{Bi}_2\text{E}_3$ (E = S, Se, and Te) hierarchitectures: The case of $\text{Bi}_2\text{S}_3$ with superior visible-light-driven Cr(VI) photoreduction capacity



Runming Wang<sup>a,1</sup>, Gang Cheng<sup>a,1</sup>, Zan Dai<sup>a</sup>, Jie Ding<sup>a</sup>, Yunling Liu<sup>b</sup>, Rong Chen<sup>a,\*</sup>

<sup>a</sup>School of Chemistry and Environmental Engineering and Key Laboratory for Green Chemical Process of Ministry of Education, Wuhan Institute of Technology, Xiongchu Avenue, Wuhan 430073, PR China

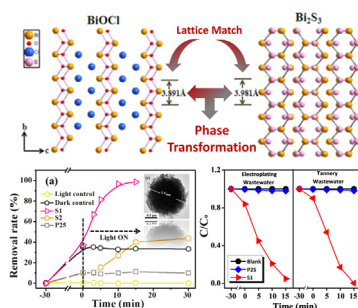
<sup>b</sup>State Key Laboratory of Inorganic Synthesis and Preparative Chemistry, College of Chemistry, Jilin University, Changchun 130012 PR China

## HIGHLIGHTS

- $\text{Bi}_2\text{S}_3$  hierarchical nanostructures (HNs) were fabricated by a combined synthetic strategy.
- A topotactic transformation from  $\text{BiOCl}$  microsphere to  $\text{Bi}_2\text{S}_3$  HNs was proposed.
- $\text{Bi}_2\text{S}_3$  HNs displayed superior visible-light-driven Cr(VI) photoreduction capacity.
- $\text{Bi}_2\text{S}_3$  HNs were used for Cr(VI) removal in actual electroplating and tannery wastewater.

## GRAPHICAL ABSTRACT

$\text{Bi}_2\text{S}_3$  hierarchitectures were fabricated by a ionic-assisted microwave-ultrasonic combined synthetic strategy and exhibited superior Cr(VI) photoreduction capacity in real industrial wastewater under visible light irradiation.



## ARTICLE INFO

### Article history:

Received 24 March 2017  
Received in revised form 26 May 2017  
Accepted 21 June 2017  
Available online 22 June 2017

### Keywords:

Hierarchitectures  
 $\text{Bi}_2\text{S}_3$   
Ionic liquid  
Cr(VI)  
Photoreduction

## ABSTRACT

A general ionic-assisted microwave-ultrasonic combined synthetic strategy was developed to fabricate  $\text{Bi}_2\text{E}_3$  (E = S, Se, and Te) hierarchitectures. To understand the crystal phase transformation and morphological evolution of  $\text{Bi}_2\text{S}_3$  hierarchitectures, the fabrication of  $\text{Bi}_2\text{S}_3$  hierarchitectures was investigated by varying sulfidation time and chlorination time. A topotactic transformation from  $\text{BiOCl}$  microsphere to  $\text{Bi}_2\text{S}_3$  hierarchitectures was proposed. It was found that the structure, size, and morphology of  $\text{Bi}_2\text{S}_3$  hierarchitectures could be delicately engineered by varying chlorination time, alkyl chain length, and concentration of ionic liquid. Moreover, the as-prepared  $\text{Bi}_2\text{S}_3$  hierarchitectures displayed superior capacity of Cr(VI) photoreduction to P25 and irregular  $\text{Bi}_2\text{S}_3$  nanostructures under visible light irradiation. Effects of morphology, pH value of reaction system, Cr(VI) concentration, and catalyst dosage on the Cr(VI) photoreduction capacity of  $\text{Bi}_2\text{S}_3$  hierarchitectures were also discussed. The enhancement of photoreduction capacity is not only attributed to the intrinsic good electron transfer ability of  $\text{Bi}_2\text{S}_3$ , but also to synergistic effects of special architectures, wide photoresponse range, high light photoadsorption, high BET surface area and good electron-hole separation performance. The systematic condition experiments and Cr(VI) photoreduction in electroplating and tannery wastewater experiments further demonstrated that the hierarchical  $\text{Bi}_2\text{S}_3$  nanospheres can be used in the actual Cr(VI)-containing wastewater treatment.

© 2017 Elsevier B.V. All rights reserved.

\* Corresponding author.

E-mail address: rchenhku@hotmail.com (R. Chen).

<sup>1</sup> These authors make equal contribution to this work.

## 1. Introduction

Hierarchical semiconductors self-assembled by low dimensional nanostructures have offered unprecedented prominence for photocatalysis system, since it displays higher surface area, faster carriers transfer ability, and better light multiple scattering and absorption properties, which are beneficial for photocatalytic reaction [1]. Therefore, rational design and synthesis towards highly efficient hierarchitectures photocatalyst has always been a concern and attracted considerable attention and research interest. For example, hierarchical bismuth-based nanostructures including BiOOH [2], BiOCl [3],  $(\text{BiO})_2\text{CO}_3$  [4], and  $\text{Bi}_2\text{MoO}_6$  [5] exhibiting eminent photocatalytic activities have already been reported in the past decade.

Nevertheless, the impact on photocatalysis performance, given its complexity, not only relates to morphology and structure but also to the intrinsic nature of such photocatalyst material. For example, BiOCl hierarchical structures show superior photocatalytic performance for rhodamine B (RhB) degradation, [6] but cannot be used as efficient photocatalysts for photocatalytic degradation of methyl orange (MO) or salicylic acid (SA) [7]. ZnO exhibited high photocatalytic activity for inactivating *E. coli*, but low activity for methylene blue (MB) [8], phenol [9], and 4-chlorophenol photodegradation [10]. Hence, the key issue to improve photocatalysis performance for degradation of a certain pollutant resides not merely in tailoring of structure and morphology, but also in employing a kind of proper photocatalytic material. Accordingly, it is reasonable to design a certain type of photocatalysis material that serves to be intrinsically suitable for photoinduced removal of a given pollutant, and subsequently conduct structural and morphological optimization over such a photocatalyst, and finally achieve the goal of taking full advantage of the photocatalyst. Although multitudinous works have been achieved, it still remains a great challenge.

Bismuth sulfide ( $\text{Bi}_2\text{S}_3$ ) is a photoresponsive semiconductor with a narrow bandgap ( $\sim 1.3$  eV), but it shows barely photocatalytic activity of organic pollutants [11–14], which was probably ascribed to the intrinsic nature of  $\text{Bi}_2\text{S}_3$ . In recent years,  $\text{Bi}_2\text{S}_3$ -involving composites or hybrids such as  $\text{Bi}_2\text{S}_3/(\text{BiO})_2\text{CO}_3$  [15],  $\text{Bi}_2\text{S}_3/\text{BiOCl}$  [11],  $\text{Bi}_2\text{S}_3/\text{Bi}_2\text{WO}_6$  [16],  $\text{Bi}_2\text{S}_3/\text{CuS}$  [13],  $\text{Bi}_2\text{S}_3/\text{MoS}_2$  [17],  $\text{Bi}_2\text{S}_3/\text{Bi}_2\text{O}_3$  [18],  $\text{Bi}_2\text{S}_3/\text{ZnO}$  [14],  $\text{Bi}_2\text{S}_3/\text{WO}_3$  [19], and  $\text{Bi}_2\text{S}_3/\text{BiVO}_4$  [20,21] have been widely used as multicomponent photocatalysts, in which  $\text{Bi}_2\text{S}_3$  contributes to extending photoreponse range, rectifying charge transport, and exerting accumulative catalytic effect because of its narrow band gap, high absorption coefficient, and reasonable incident photon to electron conversion efficiency [22,23]. However, most of the synthesis strategies to such composited photocatalysts involve tedious procedures and complicated technics. On the other hand, considering eminent optoelectronic characteristic of pure  $\text{Bi}_2\text{S}_3$  and excellent photocatalysis performance of 3D hierarchical nanostructures, it is of significance to dig into potential application of single-component  $\text{Bi}_2\text{S}_3$  hierarchitectures for removal of other pollutants, such as Cr(VI), which is one of toxic metal ions from nature water and can cause severe health problems. As a matter of fact, less attention has been paid on this issue, rather than the fabrication of  $\text{Bi}_2\text{S}_3$  hierarchitectures.

Recently, ionic-liquid (IL)-assisted method and microwave-assisted heating technique have been considered as effective approaches to prepare  $\text{Bi}_2\text{S}_3$  hierarchitectures due to their advantages in comparison with conventional hydrothermal/solvothermal method [11,24–27]. As a ‘designer solvent’, ILs have unique properties such as low vapor pressure, good ionic conductivity, thermal stability, dissolving ability, and microwave absorbing ability. As an effective tool, microwave dielectric heating reduces reaction time, boosts product yield, and increases product purity [28].

Meanwhile, in the fabrication of nanomaterials, ultrasound irradiation has advantages of accelerating primary nucleation, initiating secondary nucleation at relatively low supersaturation level, and improving the yields, purity, and uniformity of products [29]. However, the combined use of the two methods has been sparingly reported for the fabrication of  $\text{Bi}_2\text{S}_3$  hierarchitectures.

Herein, a microwave-ultrasonic combined irradiation route was employed to synthesize  $\text{Bi}_2\text{S}_3$  hierarchitectures, in which IL was used as the reaction medium. A topotactic phase transformation and morphological evolution from BiOCl microsphere to  $\text{Bi}_2\text{S}_3$  hierarchitectures was investigated based on the XRD, SEM, and TEM observations. The influences of the alkyl chain length and concentration of ionic liquid on the size and morphology of  $\text{Bi}_2\text{S}_3$  product were also discussed. Moreover, the as-prepared  $\text{Bi}_2\text{S}_3$  hierarchitectures showed wide photoresponse range, high photoabsorption, satisfactory separation performance and high BET specific area, leading to a good activity for the Cr(VI) photoreduction. More importantly, it was speculated that the intrinsic good electron transfer ability of  $\text{Bi}_2\text{S}_3$  materials gives rise to their photocatalytic performance. Given good photocatalytic activity and recyclability, the as-prepared  $\text{Bi}_2\text{S}_3$  hierarchitectures show great potential as a suitable photocatalyst for the reduction of Cr(VI). For practical application in real Cr(VI)-containing wastewater treatment, the effects of different interfering factors on Cr(VI) photoreduction efficiency of  $\text{Bi}_2\text{S}_3$  hierarchitectures for actual electroplating and tannery industry wastewater treatment were also discussed.

## 2. Experimental

### 2.1. Materials

Bismuth nitrate pentahydrate ( $\text{Bi}(\text{NO}_3)_3 \cdot 5\text{H}_2\text{O}$ ), potassium bichromate ( $\text{K}_2\text{Cr}_2\text{O}_7$ ), sodium bicarbonate ( $\text{NaHCO}_3$ ), thiourea (Tu), and ascorbic acid (AA) were purchased from Aladdin. Ethylene glycol (EG) and sodium oxalate ( $\text{Na}_2\text{C}_2\text{O}_4$ ) were obtained from Sinopharm Chemical Reagent Co. (China). Ionic liquid 1-hexadecyl-3-methylimidazolium chloride ( $[\text{C}_{16}\text{Mim}]\text{Cl}$ ), 1-decyl-3-methylimidazolium chloride ( $[\text{C}_{10}\text{Mim}]\text{Cl}$ ), and 1-butyl-3-methylimidazolium ( $[\text{BMim}]\text{Cl}$ ) were purchased from Shanghai Chengjie Chemical Co. Ltd (China). Silver nitrate ( $\text{AgNO}_3$ ) was purchased from Aldrich (USA). All chemicals were analytical grade and used directly without further purification. Distilled and deionized water were used throughout this work.

The two kinds of actual industry wastewater used in the Cr(VI) photoreduction experiments were obtained from local actual electroplating and tannery plants (Wuhan, Hubei, China), respectively. The wastewater was used without any purification.

### 2.2. Preparation of $\text{Bi}_2\text{S}_3$ hierarchitectures

$\text{Bi}_2\text{S}_3$  hierarchitectures were fabricated via a combined microwave-ultrasonic irradiation method. In a typical synthetic procedure, 1 mmol  $[\text{C}_{16}\text{Mim}]\text{Cl}$  was first dissolved in 25 mL EG at 70 °C under vigorous magnetic stirring. The solution was then mixed with another 25 mL EG containing 1 mmol  $\text{Bi}(\text{NO}_3)_3 \cdot 5\text{H}_2\text{O}$  and sonicated till all chemicals were well-dispersed. Subsequently, the mixed solution was transferred to a microwave reactor (XH-300A, Beijing Xianghu Technology Co., Ltd.) and heated up to 180 °C within 3 min under microwave (800 W) and discontinuous ultrasonic (500 W, 2 s insonation and 1 s interruption) irradiation and then this reaction system was maintained for 15 min. This duration was denoted as chlorination. After that, 10 mL EG containing 2 mmol Tu was rapidly added into the reaction system within 15 min irradiation. Thereafter the reactor was maintained under the same condition for another 15 min, which was denoted

as sulfidation. After cooling down to room temperature, the resultant black product was secured by centrifugation and washed with deionized water and absolute ethanol for ten times. The final product was dried in a desiccator for further characterization. Other samples were prepared using the same method by varying several experimental parameters. The detailed experimental parameters were listed in Table 1. It is important to note that AA was used as a reductant in the synthesis of  $\text{Bi}_2\text{Se}_3$  ( $S_{\text{BiSe}}$ ) and  $\text{Bi}_2\text{Te}_3$  ( $S_{\text{BiTe}}$ ).

### 2.3. Characterization

X-ray powder diffraction (XRD) was carried out on Bruker axS D8 Discover ( $\text{Cu K}\alpha = 1.5406 \text{ \AA}$ ). The scanning rate is  $1^\circ \text{ min}^{-1}$  in the  $2\theta$  range from 10 to 80 degrees. Scanning electron microscopy (SEM) images were taken on a Hitachi S4800 scanning electron microscope operating at 5.0 kV. Transmission electron microscopy (TEM) images, energy dispersive X-ray (EDX) spectrum, and selected-area electron diffraction (SAED) patterns were recorded on a Philips Tecnai 20 electron microscope at an accelerating voltage of 200 kV. Samples for TEM analysis were prepared by drying a drop of a nanocrystal dispersion in absolute ethanol on carbon-coated copper grids. UV–vis diffuse reflectance spectra (DRS) were recorded on a UV–vis spectrometer (Shimadzu UV-2550) by using  $\text{BaSO}_4$  as a reference and were converted from reflection to absorbance by the Kubelka-Munk method. Brunauer-Emmett-Teller (BET) specific surface area of the powders was analyzed by nitrogen adsorption in a Micromeritics ASAP 2020 nitrogen adsorption apparatus (USA). X-ray photoelectron spectra (XPS) of the catalysts were performed in a VG Multilab2000 spectrometer by using  $\text{Al K}\alpha$  (1486.6 eV) radiation as the source. Photoluminescence (PL) spectra were recorded on a Shimadzu RF-5301PC fluorescence spectrophotometer. The Raman spectra were recorded using a Horiba Jobin-Yvon LabRam HR800 Raman microspectrometer, with an excitation laser at 514 nm. Electrochemical impedance spectroscopy (EIS) measurements were performed on a CHI 760B electrochemical workstation (Shanghai Chenhua Inc., China) with a conventional three-electrode system at room temperature in air. The Zeta potential of the sample was measured by using a Zeta-Meter (Zetasizer 90, Malvern).

### 2.4. Photocatalytic activity measurements

Photocatalytic activities of the as-prepared samples were examined by the photocatalytic reduction of Cr(VI) under visible light irradiation by a 500 W Xe lamp with a 400 nm cutoff filter. In a typ-

ical experiment, 0.02 g prepared  $\text{Bi}_2\text{S}_3$  sample was added into a cylindrical glass vessel surrounded by a circulating water jacket, which contained 25 mL Cr(VI) solution. Prior to irradiation, the suspensions were stirred in the dark for 0.5 h to ensure adsorption-desorption equilibrium. Subsequently the solution was exposed to visible light irradiation under magnetic stirring. At regular intervals, 2 mL of suspension was withdrawn and centrifuged to remove catalyst particles. The concentration of Cr(VI) during the degradation was monitored by colorimetry using a LB-UV2800 spectrophotometer (China). All of the measurements were carried out at room temperature. Other photocatalytic experiments in this work were carried out over different  $\text{Bi}_2\text{S}_3$ ,  $\text{BiOCl}$ , and  $\text{TiO}_2$  powder (Degussa P25) samples under identical condition, and over the same  $\text{Bi}_2\text{S}_3$  hierarchical structure sample under different experimental conditions (initial Cr(VI) concentration from 40, 60, 80 to 100 mg/L, initial catalyst concentration from 0.5, 0.75, 1 to 1.5 g/L, and pH value from 2, 3, 4, 5, 7, 8, 9 to 11).

## 3. Results and discussion

### 3.1. Structural and morphological analysis of $\text{Bi}_2\text{S}_3$ hierarchical structure

The phase and chemical composition of the as-prepared sample (S1) were characterized by X-ray powder diffraction (XRD) measurement. Fig. 1 shows the XRD pattern of the as-synthesized product. As can be seen, all the diffraction peaks could be readily assigned to a pure orthorhombic phase of  $\text{Bi}_2\text{S}_3$  with cell constants of  $a = 11.137 \text{ \AA}$ ,  $b = 11.297 \text{ \AA}$ ,  $c = 3.981 \text{ \AA}$  (JCPDS card No. 89-8964). The intensive diffraction peaks indicate high degree of crystallinity, which was estimated to be 83.58% according to the formula given below:

$$\text{Crystallinity}(\%) = 1 - \frac{I_a}{I_{\text{sum}}} \quad (1)$$

where  $I_a$  and  $I_{\text{sum}}$  stand for the intensity of amorphous peak and total peak intensity, respectively. No peaks in the diffractograms are detected for impurities such as  $\text{BiOCl}$ . All the diffraction peaks are relatively broad, indicative of the high purity and existence of small particles of  $\text{Bi}_2\text{S}_3$ . The average crystal size of the as-prepared products was calculated to be 20.7 nm based on the Scherrer equation (detailed calculation was shown in supplementary information).

The chemical composition of S1 was confirmed by energy dispersive X-ray (EDX) analysis. As shown in Fig. 1b, the atomic ratio of Bi to S estimated to be 2:3 (Bi: 19.21%, S: 29.95%), which is consistent with the stoichiometric ratio of  $\text{Bi}_2\text{S}_3$ , while the Cu and C

**Table 1**  
Samples and the corresponding experimental parameters.

Sample	Ionic liquid	Chalcogen source	Chlorination time (min)	Sulfidation time (min)	Molar ratio of $\text{Bi}(\text{NO}_3)_3$ , ionic liquid and Chalcogen source
S1	[C <sub>16</sub> Mim]Cl	Tu	15	15	1:1:2
S2	[C <sub>16</sub> Mim]Cl	–	15	–	1:1:0
S3	[C <sub>16</sub> Mim]Cl	Tu	15	0.5	1:1:2
S4	[C <sub>16</sub> Mim]Cl	Tu	15	1	1:1:2
S5	[C <sub>16</sub> Mim]Cl	Tu	15	5	1:1:2
S6	[C <sub>16</sub> Mim]Cl	Tu	15	10	1:1:2
S7	[C <sub>16</sub> Mim]Cl	Tu	0.5	15	1:1:2
S8	[C <sub>16</sub> Mim]Cl	Tu	1	15	1:1:2
S9	[C <sub>16</sub> Mim]Cl	Tu	5	15	1:1:2
S10	[C <sub>16</sub> Mim]Cl	Tu	10	15	1:1:2
S11	[C <sub>10</sub> Mim]Cl	Tu	15	15	1:1:2
S12	[C <sub>4</sub> Mim]Cl	Tu	15	15	1:1:2
S13	–	Tu	–	15	1:1:2
S14	[C <sub>16</sub> Mim]Cl	Tu	15	15	0.5:1:2
S15	[C <sub>16</sub> Mim]Cl	Tu	15	15	2:1:2
$S_{\text{BiSe}}$	[C <sub>16</sub> Mim]Cl	Se	15	15	1:1:2
$S_{\text{BiTe}}$	[C <sub>16</sub> Mim]Cl	$\text{TeO}_2$	15	15	1:1:2

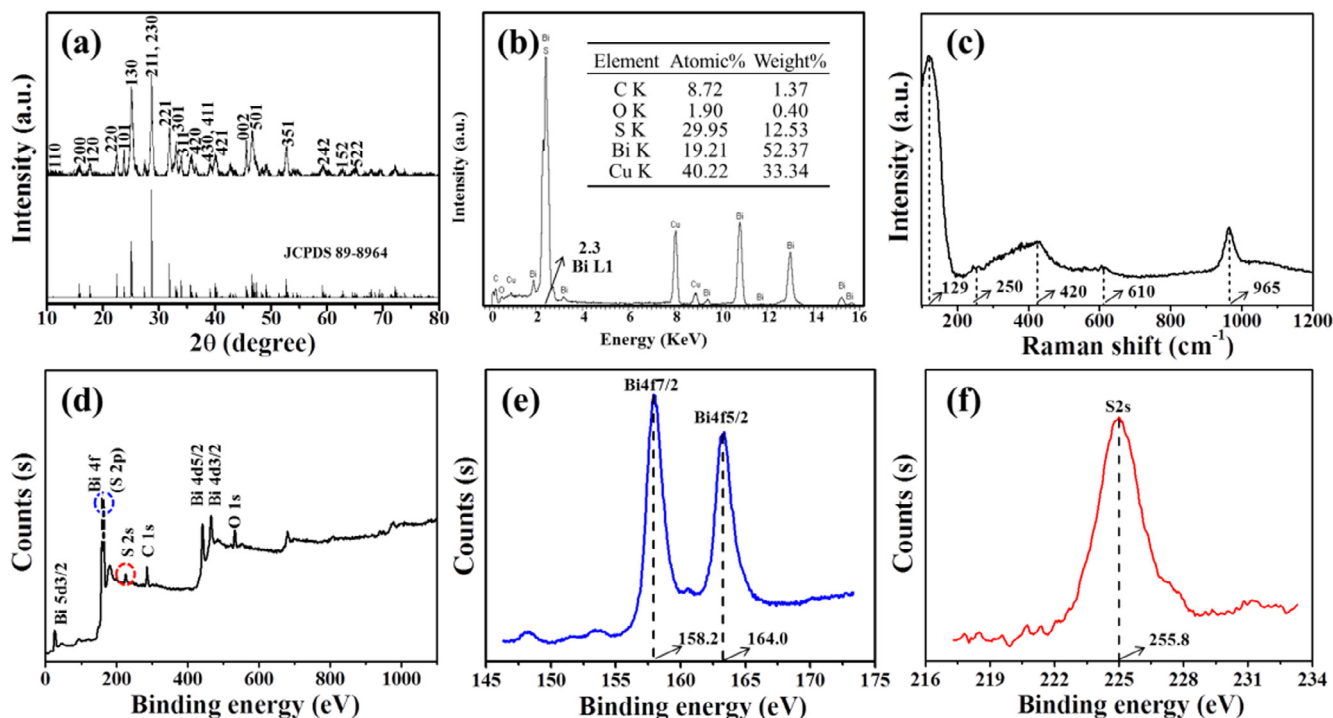


Fig. 1. (a) XRD pattern; (b) EDX spectrum; (c) Raman spectrum; (d–f) XPS spectrum of  $\text{Bi}_2\text{S}_3$  (S1). The inset in (b) shows the table of chemical composition.

signals come from test grid, and O signal comes from atmosphere. The Raman spectroscopy was employed to further confirm the fabrication of  $\text{Bi}_2\text{S}_3$ . Fig. 1c shows the typical Raman spectrum of the products recorded between 100 and  $1200\text{ cm}^{-1}$ , with five bands located at about 129, 250, 420, 610 and  $965\text{ cm}^{-1}$  belonging to orthorhombic phase of  $\text{Bi}_2\text{S}_3$ , which accord well with previous reports of  $\text{Bi}_2\text{S}_3$  prepared by biomolecule-assisted soft chemistry route and ultrasonic spray pyrolysis technique [30,31]. The chemical states of surface elements in  $\text{Bi}_2\text{S}_3$  products were also identified by X-ray photoelectron spectroscopy (XPS) analysis. The XPS survey spectra of the  $\text{Bi}_2\text{S}_3$  products is shown in Fig. 1d, and the characteristic energy peaks of two kinds of atoms, i.e., bismuth and sulfide, can be observed in the spectra. The two strong peaks at 158.2 and 164.0 eV in Fig. 1e were assigned to  $\text{Bi}4f_{7/2}$  and  $\text{Bi}4f_{5/2}$ , respectively, corresponding to  $\text{Bi}^{3+}$  [32–34]. The intense peak at 225.8 eV assigning to S2s in Fig. 1f belongs to  $\text{S}^{2-}$  in a bismuth-sulfide bond in  $\text{Bi}_2\text{S}_3$ . Therefore, it was concluded that pure and well-crystalline orthorhombic-phase  $\text{Bi}_2\text{S}_3$  has been successfully fabricated via the microwave-ultrasonic combined synthesis approach.

The structure and morphology of the products were investigated by SEM, TEM, HRTEM, and SAED. Fig. 2a and b show the typical SEM images of the as-prepared  $\text{Bi}_2\text{S}_3$ . It can be clearly seen that the  $\text{Bi}_2\text{S}_3$  products (S1) mainly comprised of hierarchical microspheres with diameter of 1.2–2.5  $\mu\text{m}$ . The high-magnification image (Fig. 2b) reveals that the spherical architecture is constructed by incompletely interwoven nanorods with diameters of less than 100 nm. A TEM image analysis (Fig. 2c) further shows that the products consisted of well-defined spherical structures having a solid inside and porous exterior. Fig. 2d shows a HRTEM image recorded from one area of the outside of a microsphere, in which nanorods with diameters of about 20 to 45 nm connecting to each other can be observed. It indicated that the entire  $\text{Bi}_2\text{S}_3$  architectures consisted of a solid center and a porous surface assembled with nanorods, which agreed well with the SEM observation. Fig. 2e shows a single  $\text{Bi}_2\text{S}_3$  nanorod having a diameter of

about 40 nm. Fig. 2f displays a HRTEM image of an individual  $\text{Bi}_2\text{S}_3$  nanorod, where the fringe spacing of 0.199 nm assigns well with the spacing of (002) lattice plane of  $\text{Bi}_2\text{S}_3$  orthorhombic phase. The diffraction spots of the corresponding SAED pattern of (Inset in Fig. 2f) can be indexed as the (120) and (002) lattice planes of  $\text{Bi}_2\text{S}_3$ , and the angle between (120) and (002) planes being about  $90^\circ$  matches well with theoretical value, indicating a c-axis direction growth of the nanorod. The HRTEM and SAED results revealed that the  $\text{Bi}_2\text{S}_3$  spherical architectures were constructed by single crystal nanorods growing along the [001] direction.

This synthetic method can be developed and employed to prepare other hierarchy nanostructure of bismuth chalcogenide. Upon the replacement of Tu with Se powder in the reaction system, the XRD pattern (Fig. 3a) shows that  $\text{Bi}_2\text{Se}_3$  product was obtained. As depicted in Fig. 3b–d, the  $\text{Bi}_2\text{Se}_3$  sample confirms spherical morphology, and  $\text{Bi}_2\text{Se}_3$  (S16) microspheres consist of thick nanosheets. While  $\text{TeO}_2$  was employed to substitute Tu, as shown in Fig. 3e–h, it was observed that  $\text{Bi}_2\text{Te}_3$  (S17) spherical architectures composed of many small nanosheets were fabricated. On the basis of the above results, it can be concluded that it is a general and an efficient synthetic strategy to prepare  $\text{Bi}_2\text{E}_3$  ( $\text{E} = \text{S}, \text{Se}, \text{and Te}$ ) hierarchy nanostructures using an ionic liquid-involved microwave-ultrasonic combined route employed in the present system.

### 3.2. Growth, size, and morphology controll of $\text{Bi}_2\text{S}_3$ hierarchy structure

To investigate the formation process of  $\text{Bi}_2\text{S}_3$  hierarchy structure, a series of comparison experiments were performed. First of all, we collected the white precipitate formed prior to the addition of Tu addition. The XRD pattern (Fig. 4a) indicates that the product (S2) are pure tetragonal phase bismuth oxychloride (JCPDS Card 6–649:  $a = 3.891\text{ \AA}$  and  $c = 7.369\text{ \AA}$ , space group P4/nmm), which means  $\text{BiOCl}$  precursor formed at the initial stage. As illustrated from the SEM image in Fig. 4b, the as-obtained  $\text{BiOCl}$  precursor is

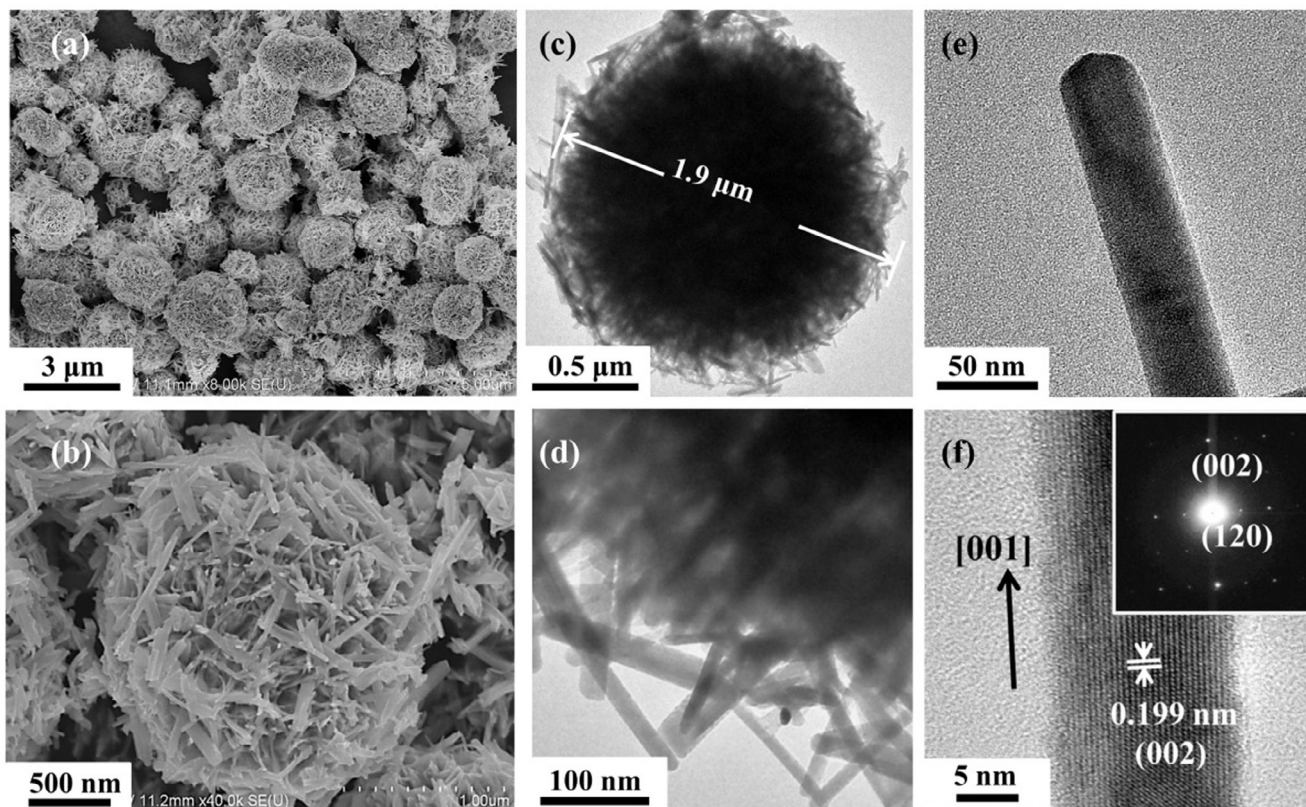


Fig. 2. (a and b) SEM, (c, d, and e) TEM, (f) HRTEM images, and corresponding SAED pattern (inset of f) of  $\text{Bi}_2\text{S}_3$  hierarchitectures (S1).

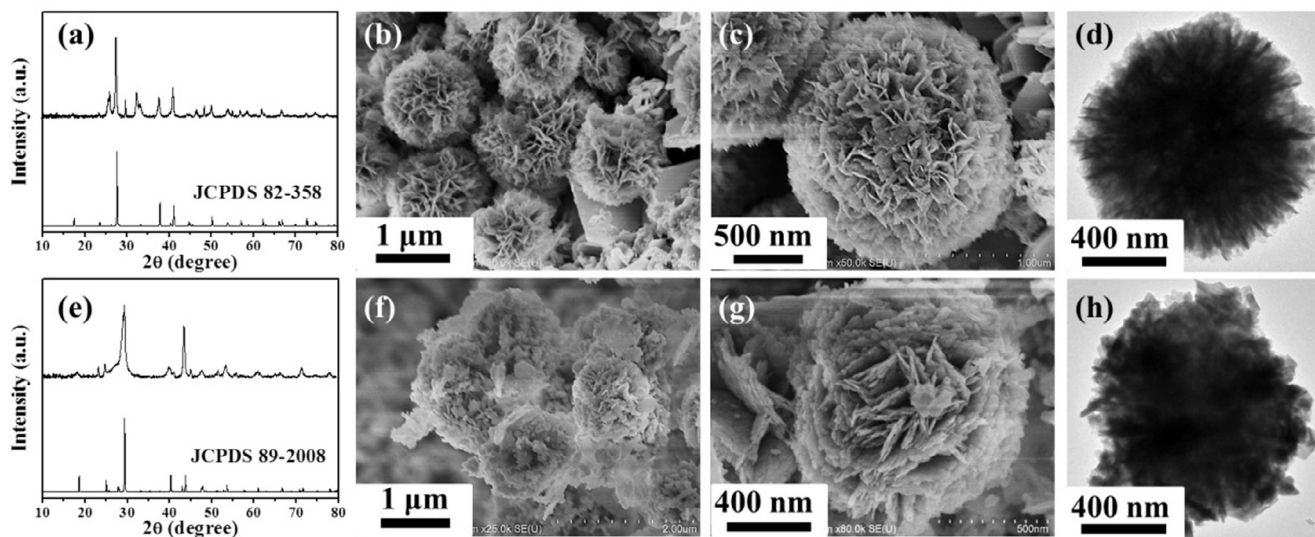


Fig. 3. XRD pattern, SEM, and TEM images of different bismuth chalcogenide hierarchitectures: (a–d)  $\text{Bi}_2\text{Se}_3$ ; (e–h)  $\text{Bi}_2\text{Te}_3$ .

composed of well-defined flower-like microspheres with diameters of c.a.  $1.5 \mu\text{m}$ . The enlarged SEM (inset of Fig. 4b) and TEM (Fig. 4c and d) images revealed that the microspheres were constructed by loose-packed nanoflakes. Fig. 4e shows an HRTEM image recorded from the edge of the nanoflake indicated in Fig. 4d. The lattice fringe with spacing of  $\sim 0.273 \text{ nm}$  corresponded to the  $d$ -spacing of (110) planes of  $\text{BiOCl}$ , which was perpendicular to the  $c$  axis. The sharp spots in the corresponding SEAD pattern (inset of Fig. 4e) are ascribed to the  $c$  axis of tetragonal  $\text{BiOCl}$ , being in

accord with the intense peak of (110) plane in the corresponding XRD pattern. The retarded crystal growth along  $c$  axis might be due to the preferred adsorption of  $[\text{C}_{16}\text{Mim}]^+$  cations on  $ab$  plane [35]. Based on the above examinations, it was concluded that well-defined  $\text{BiOCl}$  microspheres constructed by nanoplates with the top face of the (001) plane were favourably fabricated before with chalcogen was added into the reaction system.

It was observed that  $\text{BiOCl}$  microspheres were obtained after 15 min chlorination, which were further evolved into

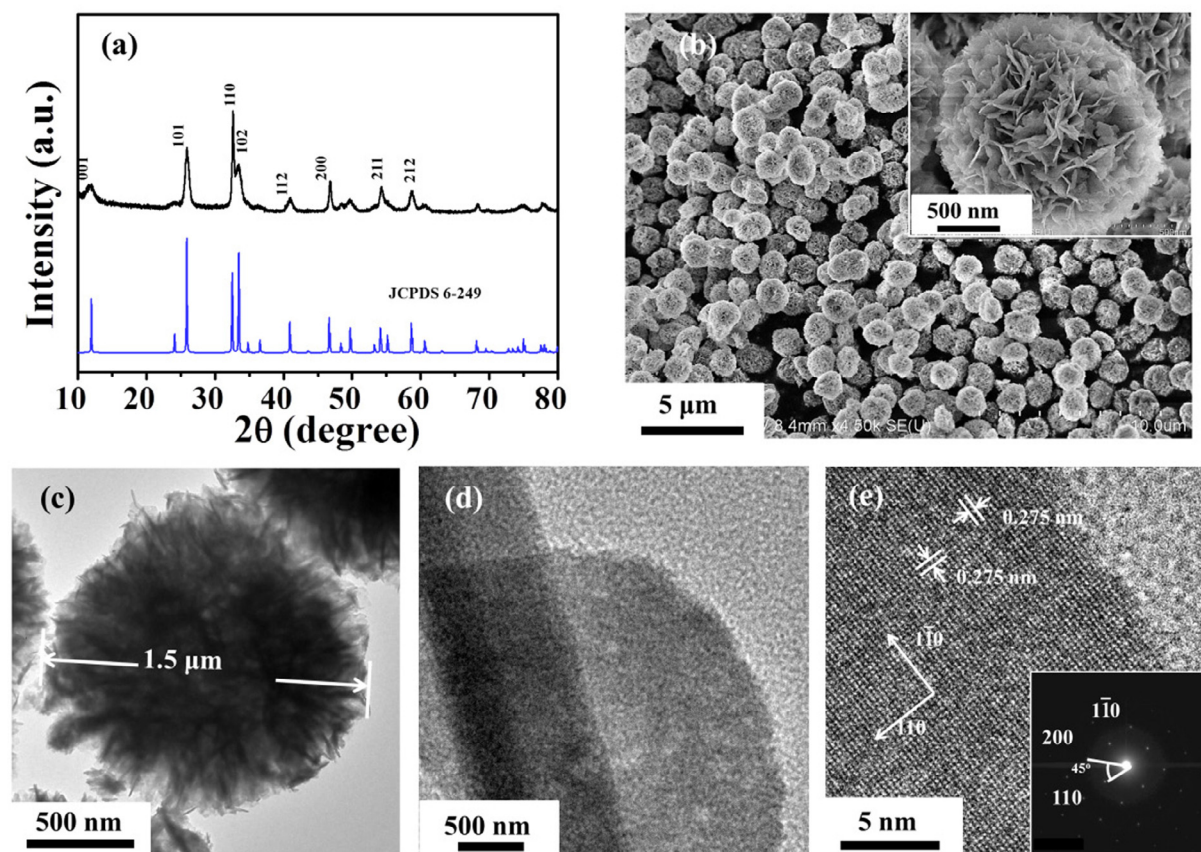


Fig. 4. (a) XRD pattern, (b) SEM, (c) TEM, and (d and e) HRTEM images, and SAED pattern (inset of e) of BiOCl (S2).

$\text{Bi}_2\text{E}_3$  (take  $\text{Bi}_2\text{S}_3$  as an example) microspheres by another 15 min sulfidation. Given those experimental results and the previous reports [2,35,36], the probable reaction processes in aqueous solution can be summarized in Eqs. (2)(4):



To understand the phase transformation and structure evolution, we carried out a time-dependent experiment by collecting intermediates at different sulfidation times. As sulfidation time increases, the topotactic transformation occurs gradually, which could be observed from SEM images (Fig. 5) and XRD patterns (Fig. S1). When the sulfidation time is 30 s, as shown in Fig. 5a and b, the initial products mainly consist of loose-packed microspheres, and some of them tend to be aggregated in the form of destroyed spheres. When the sulfidation time was increased to 1 min (Fig. 5c and d), it was observed that a large amount of quasi-spherical structures composed of small particles and thick plates were obtained. At the same time, the obtained microspheres were closed-packed. When the sulfidation time is increased to 5 min, Fig. 5e and f show that the product remain the same size and morphology of such quasi-spherical structures, however, the microspheres are assembled from plenty of nanorods but a small quantity of nanoparticles or nanoplatelets. While sulfidation time was further increased to 10 min, as can be seen in Fig. 5g and h, the microspheres were chiefly constructed by nanorods subunits, and most of them are parallel to each other. It was found that these nanorods did not have a preferential growth direction but were parallel to the plane of nanoplate, probably owing to the

epitaxial growth between the BiOCl nanoplate and the  $\text{Bi}_2\text{S}_3$  nanorod.

On the basis of the above results, we could preliminarily speculate the formation process of hierarchical  $\text{Bi}_2\text{S}_3$  nanostructures involved the phase transformation from BiOCl to  $\text{Bi}_2\text{S}_3$  and a template-induced structure evolution from nanoplates-assembled microspheres to nanorods-constructed microspheres. It is well-known that layered structure of  $\text{Bi}_2\text{S}_3$  single crystalline has weak Van der Waals forces among  $c$ -plane and strong polarization along  $c$ -axis. Accordingly,  $\text{Bi}_2\text{S}_3$  tends to grow along its  $c$ -axis forming 1-D structure. Once the sulfur ions released by Tu diffused to the surface of BiOCl nanoplate, they would promptly substitute for the pre-existed oxygen ions and chlorine ions owing to the low solubility of  $\text{Bi}_2\text{S}_3$  ( $K_{\text{sp}} = 1.0 \times 10^{-97}$ ) compared to BiOCl ( $K_{\text{sp}} = 1.8 \times 10^{-31}$ ). Then the  $\text{Bi}_2\text{S}_3$  single-crystalline formed on the top surface of the (110) plane of BiOCl and continued to grow along its  $c$ -axis, eventually generated such [001]-orientated  $\text{Bi}_2\text{S}_3$  nanorods (shown in Fig. S2). These nanorods subsequently attached to one another generating certain quasi-rodlike aggregations on the surface of microspheres so as to diminish surface area and surface energy via Ostwald ripening. Accordingly, it could be concluded that, as the chemical transformation proceeded, the BiOCl microsphere assembled by plate-like subunits served as the sacrificial template, gradually evolving into the  $\text{Bi}_2\text{S}_3$  microsphere assembled by rod-like subunits via a chemical transformation route.

Noticeably, it was found the variation on chlorination time could tailor the composition and morphology of the product. Fig. 6a and b show SEM images of the product (S7) prepared with chlorination time of 30 s. As can be seen, the product was composed of uniformly dispersive microspheres and nanorods, in which the microspheres showed a resemblance to S2 (BiOCl), being

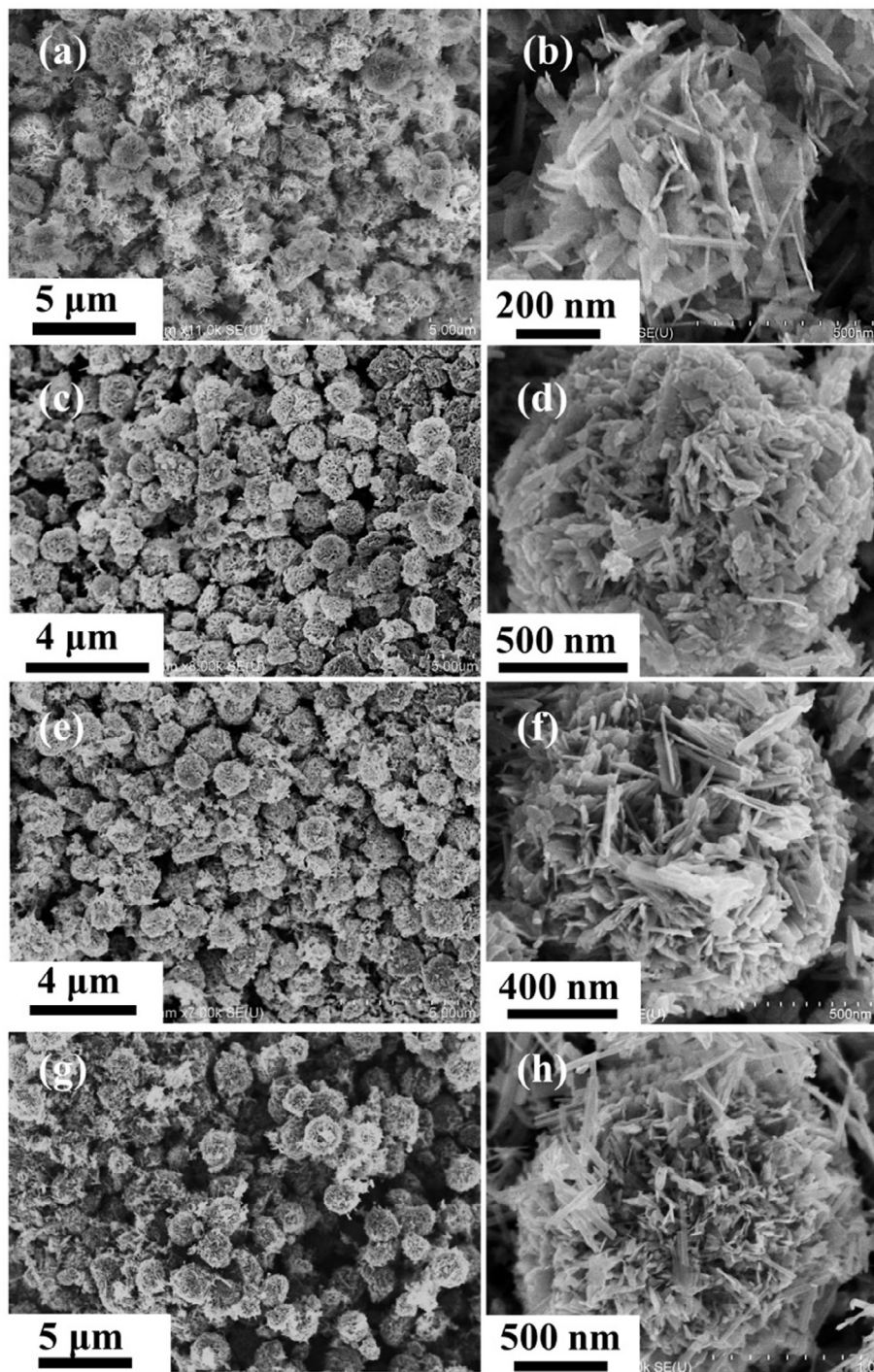


Fig. 5. SEM images of  $\text{Bi}_2\text{S}_3$  samples synthesized with different sulfidation time: (a and b) 30 s; (c and d) 1 min; (e and f) 5 min; (g and h) 10 min.

constructed by loose-packed nanoplates. In the meanwhile, the nanorods of **S7** were similar to rod-like subunits in **S1**. To be more specific, the product (**S7**) consisting of a mixture of  $\text{BiOCl}$  and  $\text{Bi}_2\text{S}_3$  could be confirmed by the corresponding XRD pattern (Fig. S3). As chlorination time was increased to 1 min,  $\text{BiOCl}$  and  $\text{Bi}_2\text{S}_3$  peaks were still observed in the XRD pattern of product (**S8**, Fig. S3b).  $\text{BiOCl}$  and  $\text{Bi}_2\text{S}_3$  appeared probably as the typical nanoplates and nanorods in Fig. 6c and d, respectively. Pure  $\text{Bi}_2\text{S}_3$  could be obtained in products with chlorination time increases to 5 and 10 min (Fig. S3c and S3d). But in Fig. 6e–h, the structures of  $\text{Bi}_2\text{S}_3$  products were changed from nanorods to microspheres when the chlorination time was increased from 5 to 10 min.

In the present system, the size of  $\text{Bi}_2\text{S}_3$  hierarchitectures could be tailored by altering the alkyl chain length of ionic liquid. When replacing  $[\text{C}_{16}\text{MIM}]\text{Cl}$  with  $[\text{C}_4\text{Mim}]\text{Cl}$  and  $[\text{C}_{10}\text{Mim}]\text{Cl}$ ,  $\text{Bi}_2\text{S}_3$  hierarchitectures with diameter of ca. 1.4  $\mu\text{m}$  (**S11**) and ca. 1.1  $\mu\text{m}$  (**S12**) were obtained, respectively, both of which are smaller than that of **S1** (ca. 1.9  $\mu\text{m}$ ), as displayed in SEM and TEM images (Fig. 7a–d). In other words, the size of  $\text{Bi}_2\text{S}_3$  products tended to decrease with shortening of alkyl chain length of ionic liquid, which could be due to the shrink of the framework constructed by ionic liquid. Interestingly, when ionic liquid was not involved into the reaction system, as shown in Fig. 7e and f,  $\text{Bi}_2\text{S}_3$  products presented irregular morphology, which might be due to the quick

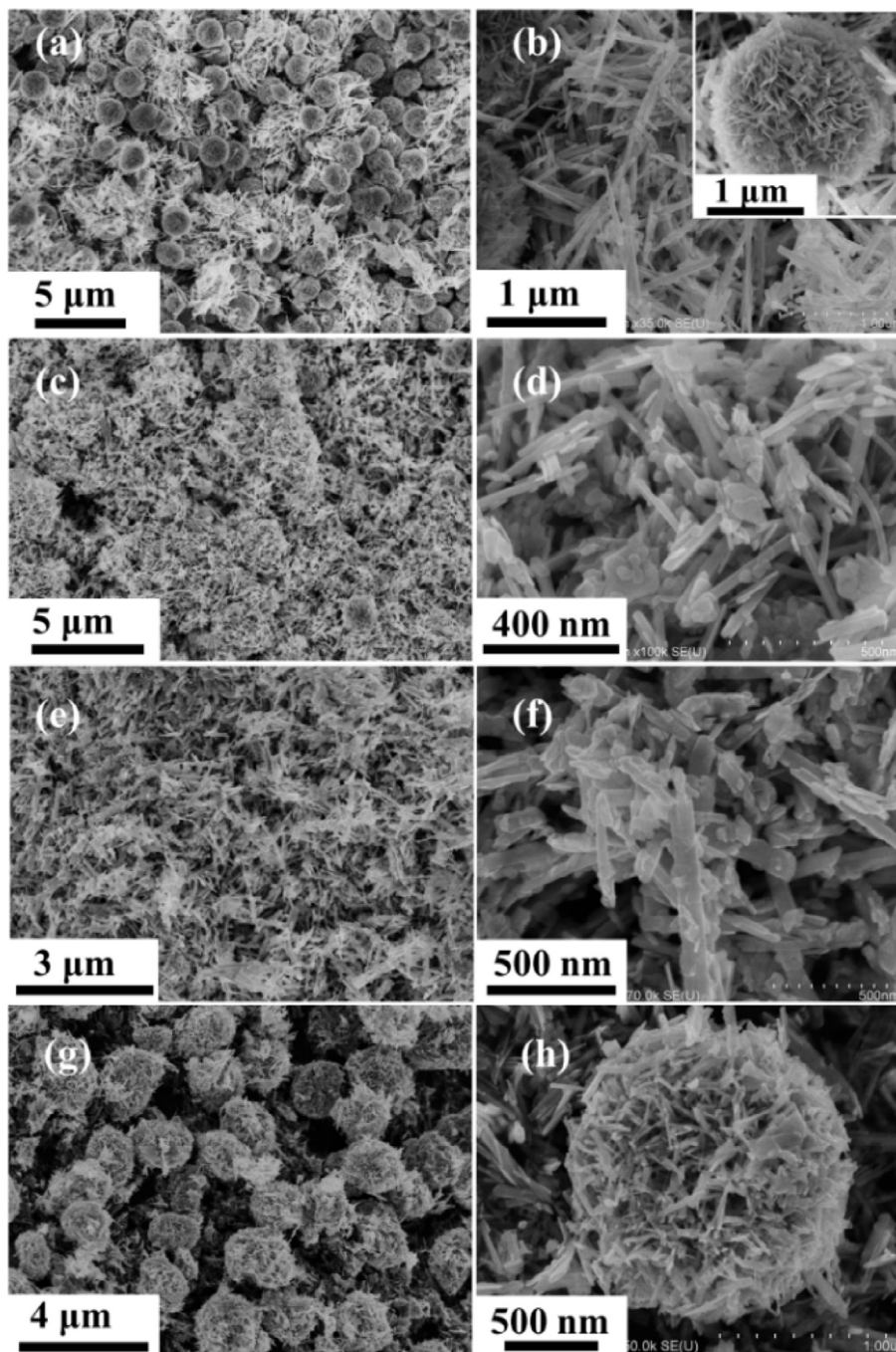


Fig. 6. SEM images of  $\text{Bi}_2\text{S}_3$  samples synthesized with different chlorination time, (a, b and inset) 30 s; (c and d) 1 min; (e and f) 5 min; (g and h) 10 min.

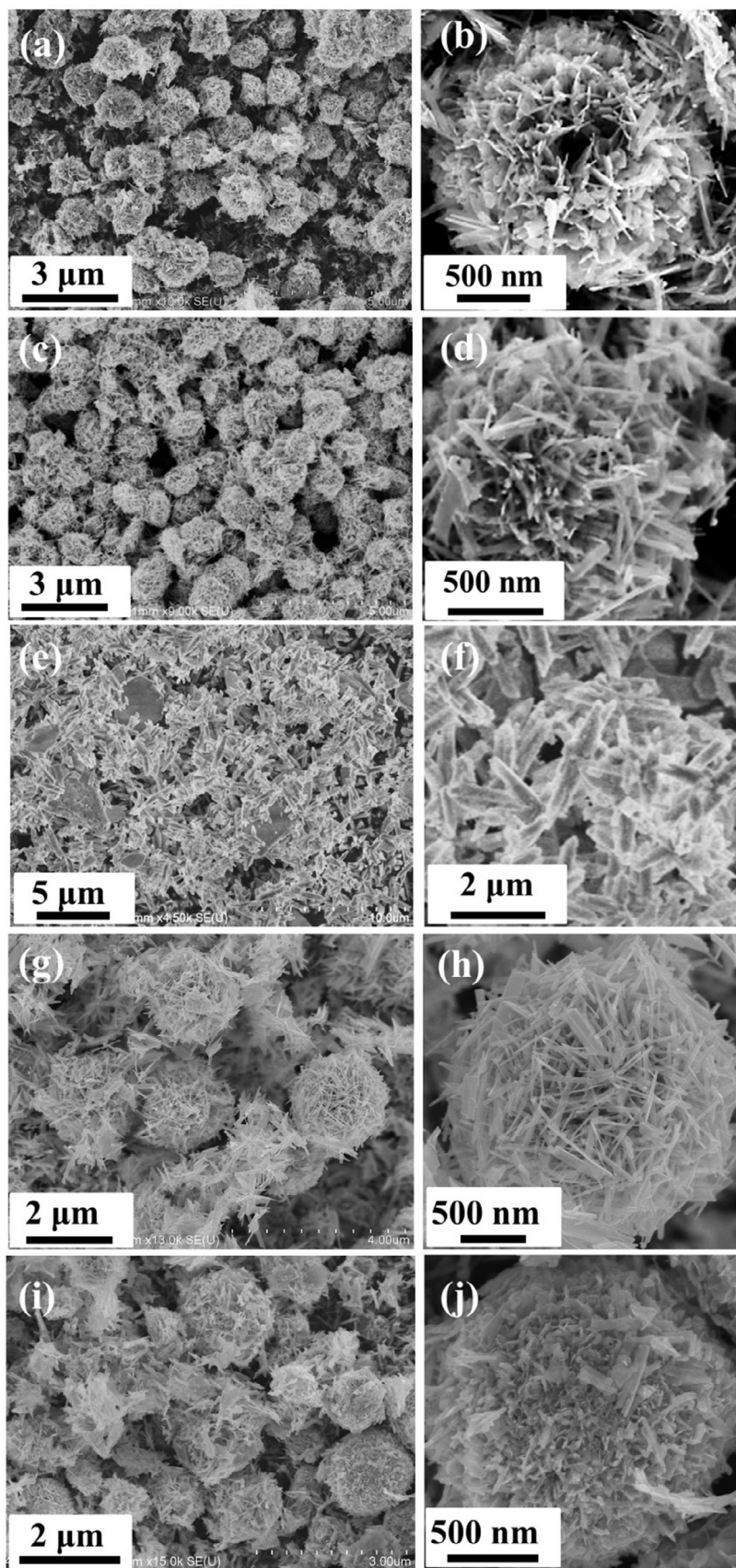
reaction of  $\text{S}^{2-}$  and  $\text{Bi}^{3+}$  in the absence of ionic liquid. In addition, the concentration of ionic liquid could modulate the aspect ratio of the subunit of  $\text{Bi}_2\text{S}_3$  hierarchy. As depicted in Fig. 6g–h, the aspect ratio of the rod-like subunit of  $\text{Bi}_2\text{S}_3$  hierarchy increases with decreasing the molar ratio of  $\text{Bi}(\text{NO}_3)_3 \cdot 5\text{H}_2\text{O} : [\text{C}_{16}\text{Mim}]\text{Cl}$  to 0.5:1 (S14), while diminished with increasing the ratio to 2:1 (S15), which might be due to the varying of chemical potential and viscosity of such reaction system by adding varying amount of ionic liquid [37].

### 3.3. BET analysis and property of $\text{Bi}_2\text{S}_3$ hierarchitectures

The nitrogen adsorption-desorption isotherms and Barrett–Joyner–Halenda (BJH) method were used to measure specific surface

areas and pore volumes of the  $\text{Bi}_2\text{S}_3$  samples. As shown in Fig. S4, the isotherms of  $\text{Bi}_2\text{S}_3$  hierarchitectures (S1, S11, S12, S14 and S15) display a type IV with a type H3 hysteresis loop in the range of 0.8–1.0  $p/p_0$ , indicating the presence of mesopores, which facilitates catalytic reaction because of providing more pathways for mass transferring. As listed in Table 2, obvious differences in both BET specific surface areas and pore volumes was observed between  $\text{Bi}_2\text{S}_3$  hierarchitectures and  $\text{Bi}_2\text{S}_3$  with irregular morphology (S13), which could be ascribable to the big difference on morphology.

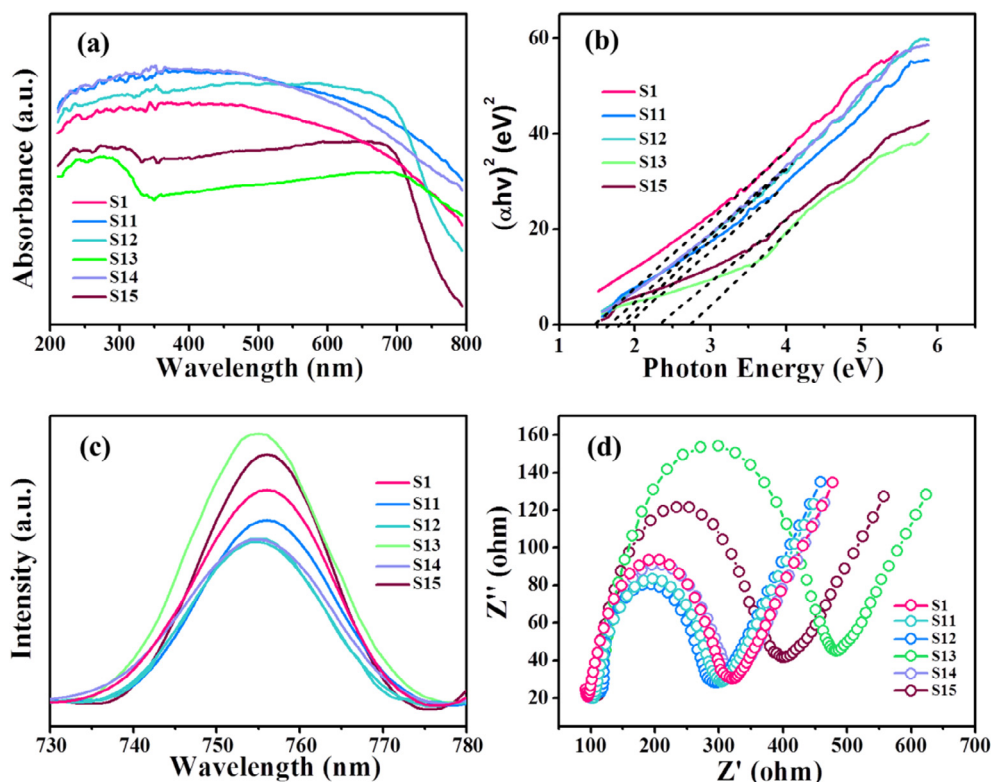
Diffuse reflectance spectroscopy (DRS) was also performed to probe the band energy structures in the range of 200–800 nm at room temperature. Fig. 8a shows a representative absorption spectrum of different  $\text{Bi}_2\text{S}_3$  samples. It was observed that the  $\text{Bi}_2\text{S}_3$  samples showed a correspondingly wide photoabsorption range,



**Fig. 7.** SEM images different Bi<sub>2</sub>S<sub>3</sub> products: (a and b) S11; (c and d) S12; (e and f) S13; (g and h) S14; (i and j) S15.

**Table 2**BET surface area ( $A_{\text{BET}}$ ), pore volumes ( $V_{\text{BJH}}$ ), crystalline size ( $D$ ) and band gap energy ( $E_{\text{g}}$ ) of different  $\text{Bi}_2\text{S}_3$  samples.

Sample	S1	S11	S12	S13	S14	S15
$A_{\text{BET}}/\text{m}^2 \text{g}^{-1}$	29.76	32.61	31.10	7.43	32.23	29.00
$V_{\text{BJH}}/\text{cm}^3 \text{g}^{-1}$	0.210	0.207	0.234	0.043	0.174	0.174
$E_{\text{g}}/\text{eV}$	1.56	2.01	1.90	2.91	1.72	2.46
$D/\text{nm}$	20.7	12.9	17.9	4.8	14.6	8.4

**Fig. 8.** (a) UV-Vis diffuse reflectance spectra; (b) The plot of  $(\alpha hv)^{1/2}$  versus  $(hv)$  curve; (c) PL spectra excited at 650 nm; (d) Nyquist plots of **S1**, **S11**, **S12**, **S13**, **S14** and **S15**.

extending to visible light region. The curves in Fig. 8b reveal that the absorption edges of  $\text{Bi}_2\text{S}_3$  samples undergo an obvious blue shift compared with  $\text{Bi}_2\text{S}_3$  bulk, probably owing to the quantum confinement effect of nanomaterials [38]. Take **S1** for instance, since its mean crystal radius (ca. 10.3 nm, calculated by Scherrer equation) is much smaller than its Bohr exciton radius (ca. 24 nm), it might cause a splitting of both the valence band (VB) and conduction band (CB) into a series of subbands, and a gap is formed between the top of the subband in the VB highest occupied molecular orbital and the bottom of the subband in the CB lowest unoccupied molecular orbital [39]. This further led to a shift in absorption edge and band gap, which could be explained on the basis of effective mass approximation model:

$$E_{\text{g}} = E_{\text{g, bulk}} + \frac{h^2}{8\mu R^2} \quad (5)$$

where  $E_{\text{g, bulk}}$ ,  $h$ ,  $\mu$  and  $R$  stand for the band gap energy of  $\text{Bi}_2\text{S}_3$  bulk crystal (ca. 1.3 eV), Planck constant, the electron and hole effective mass, and mean crystal radius, respectively. It was observed that band gap energy has a remarkable increase with the decrease of mean crystal radius. The band gap and crystalline size of all  $\text{Bi}_2\text{S}_3$  samples are summarized in Table 2.

Photoluminescence (PL) emission results from recombination of photo-induced charge carriers, which can be used to survey the fate of electron-hole pairs in semiconductor nanostructures [40].

Fig. 8c shows the PL emission spectra of different  $\text{Bi}_2\text{S}_3$  samples at room temperature. The  $\text{Bi}_2\text{S}_3$  samples has an obvious emission peak at about 755 nm, corresponding to the band gap electron-hole pairs recombination. Compared to  $\text{Bi}_2\text{S}_3$  with irregular morphology (**S13**), hierarchitectured  $\text{Bi}_2\text{S}_3$  shows a decrease in PL intensity. This suggests that the charge recombination was efficiently prevented, resulting in a higher photocatalytic activity when  $\text{Bi}_2\text{S}_3$  hierarchitectures were used as the catalysts.

Electrochemical impedance spectra (EIS) was also performed to further characterize the electron-hole separation efficiency of as-prepared  $\text{Bi}_2\text{S}_3$  catalysts. It can be seen from the Nyquist plots results (Fig. 8d) that  $\text{Bi}_2\text{S}_3$  with irregular morphology is higher than hierarchitectured  $\text{Bi}_2\text{S}_3$ , which demonstrates the faster charge transfer ability of hierarchitectured  $\text{Bi}_2\text{S}_3$  than that of irregular one. This could be contributed to effective charge separation and thereby higher electrons transporting to the surface [41]. It is worth mentioning that the charge resistance of  $\text{Bi}_2\text{S}_3$  hierarchitectures constructed by high-aspect-ratio nanorods (**S1** and **S15**) is lower than that of low-aspect-ratio nanorod (**S14**), which was attributed to the faster electron transfer along  $c$ -axis oriented material [42,43]. On the basis of the above results, it could be concluded that  $\text{Bi}_2\text{S}_3$  hierarchitectures showed high specific surface area, strong light adsorption, fast carriers transfer, and high electron-hole separation efficiency, compared to  $\text{Bi}_2\text{S}_3$  with irregular morphology.

### 3.4. Photocatalysis activity of Bi<sub>2</sub>S<sub>3</sub> hierarchitectures

The photocatalytic activity of the as-synthesized Bi<sub>2</sub>S<sub>3</sub> samples (**S1**, **S11**, **S12**, **S13**, **S14**, and **S15**) were measured on the photoreduction of Cr(VI) under visible light irradiation. The characteristic absorption of Cr(VI) at 354 nm is used to monitor the photocatalytic reduction process. For comparison, the degradation of Cr(VI) over P25, BiOCl hierarchitectures dark control (without light illumination), light control (without catalysts), and negative control (without light illumination or catalysts) were performed under identical conditions.

Fig. 9a shows the photoreduction rates of Cr(VI) over different photocatalysts under visible light irradiation. It was clearly observed that Cr(VI) concentration remained unchanged in the light control even after 30 min, but 30% of Cr(VI) was removed in the dark control within 30 min, which chiefly resulted from electrostatic attraction. However, when the light resource was switched on, the Cr(VI) solution was completely decolorized within 15 min in the presence of Bi<sub>2</sub>S<sub>3</sub> hierarchitectures (**S1**), indicating of 100% photoreduction of Cr(VI), while only 10% and 30% of Cr(VI) was removed for P25 and BiOCl (**S2**), respectively, even if the irradiation time was prolonged to 30 min. The above results demonstrated that Bi<sub>2</sub>S<sub>3</sub> hierarchitectures was an excellent photocatalyst for reduction of Cr(VI), compared with BiOCl and P25.

To investigate the relationship between the morphology and the photocatalytic activity, the photocatalysis experiments over different Bi<sub>2</sub>S<sub>3</sub> hierarchitectures were further carried out. Fig. 9b shows the photocatalytic reduction rate of Cr(VI) versus the irradiation time for the different Bi<sub>2</sub>S<sub>3</sub> photocatalysts. It was seen that Bi<sub>2</sub>S<sub>3</sub> hierarchitectures display higher photocatalytic reduction capacity of Cr(VI) than that of Bi<sub>2</sub>S<sub>3</sub> with irregular morphology (**S13**).

XRD and SEM were also used to study the chemical composition and morphology of the photocatalysts after photocatalytic reduction reaction. Fig. S5a and S5b show that the re-collected photocatalyst remain the phase of Bi<sub>2</sub>S<sub>3</sub> and the structures remain almost unchanged. XPS (Fig. S5c) was used to further examine the surface of re-collected Bi<sub>2</sub>S<sub>3</sub> catalyst after photocatalytic reduction from Cr(VI) to Cr(III). Two main peaks at 586.80 and 577.30 eV were assigned to Cr 2p<sub>1/2</sub> and Cr 2p<sub>3/2</sub> of Cr(III), respectively [44,45], corresponding to the typical characteristics of oxides or hydroxide forms of Cr(III), which confirmed the photocatalytic reduction of Cr(VI). As depicted in Raman spectra (Fig. S5d), a bond located at 823 cm<sup>-1</sup> was assigned to symmetric stretching vibration of ν<sub>1</sub> Cr(III)-O, which further demonstrates the photoreduction process of Cr(VI) to Cr(III).

It is well-known that high specific surface area, strong light absorption, and high electron-hole separation efficiency contribute

to excellent photocatalysis performance. Through the analysis of BET, PL and EIS, there could be following two reasons for the high photocatalytic activity of the Bi<sub>2</sub>S<sub>3</sub> hierarchitectures. Firstly, the Bi<sub>2</sub>S<sub>3</sub> hierarchitectures have higher surface areas, and therefore adsorb more Cr(VI) than that of irregular Bi<sub>2</sub>S<sub>3</sub> nanostructures, which allows for the more efficient transport. Secondly, the special hierarchitectures not only reduces reflection and thus harvest the light wheel, but also promotes the transfer of light-generated charge carriers to the reactive surfaces and allows the rapid diffusion of reactants and products during the reaction.

To further investigate the active species responsible for the Cr(VI) reduction, we use several scavengers to probe the specific reactive species formed during photocatalysis experiments. NaHCO<sub>3</sub>, AgNO<sub>3</sub>, and Na<sub>2</sub>C<sub>2</sub>O<sub>4</sub> was used for proton, electron, and hole scavenger, respectively. Fig. 10a shows the Cr(VI) photoreduction rates of Bi<sub>2</sub>S<sub>3</sub> hierarchitectures (**S1**) in the presence of different scavengers. It was observed that the photoreduction of Cr(VI) was greatly suppressed by the addition of NaHCO<sub>3</sub> or AgNO<sub>3</sub>, but hardly inhibited by Na<sub>2</sub>C<sub>2</sub>O<sub>4</sub>, indicating that photogenerated electrons mainly accounted for the Cr(VI) photoreduction.

The electron transfer ability could be demonstrated by the calculation of charge carrier diffusivity and migration time inside Bi<sub>2</sub>S<sub>3</sub> crystal [46]. The charge carrier diffusivity (*D*) was defined as:

$$D = \frac{\mu k_b T}{q_e} \quad (6)$$

where  $\mu$ ,  $k_b$ ,  $T$ ,  $q_e$  stand for the mobility of charge carriers, Boltzmann coefficient, absolute temperature and the charge of the electron, respectively. The mobility of electron and hole inside Bi<sub>2</sub>S<sub>3</sub> crystal at room temperature were reported to be 3487.08 and 797.51 cm<sup>2</sup>(V·s)<sup>-1</sup>, respectively [47]. Therefore the diffusivities of the photogenerated electron and hole were calculated to be  $9.0 \times 10^{-3}$  and  $2.1 \times 10^{-3}$  m<sup>2</sup>·s<sup>-1</sup>, respectively. According to calculation results, the migration time of photogenerated electrons is almost four times smaller than photogenerated hole, resulting in relatively high hole density inside the Bi<sub>2</sub>S<sub>3</sub> crystals. In other words, Bi<sub>2</sub>S<sub>3</sub> material could show its own nature when involved into the electron-consuming process, i.e. photoreduction of Cr(VI).

In addition, the photocatalytic activity of the as-prepared Bi<sub>2</sub>S<sub>3</sub> hierarchitectures (**S1**) on photoreduction of Cr(VI) in different pH values was also evaluated. Fig. 10 shows the variations on the Cr(VI) photoreduction rate, Cr(VI) adsorption rate, and zeta potential of the reaction system at different pH values. As can be seen, the Cr(VI) photoreduction and adsorption removal rates decreased with the increase of pH value. Although the Bi<sub>2</sub>S<sub>3</sub> hierarchitectures showed the lowest adsorption capacity in the alkaline condition, it still achieved 80% photoreduction rate for the Cr(VI). The isoelectric point of **S1** was estimated to be 4.52 mV based on zeta potential analysis, below which the catalyst surface was positive

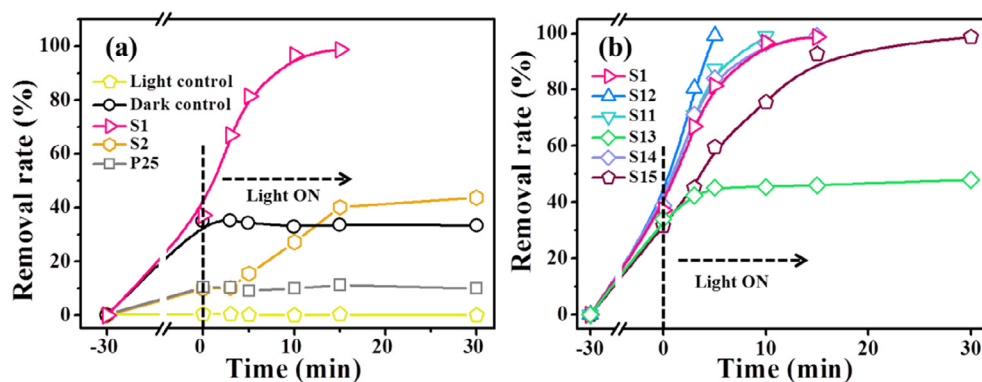
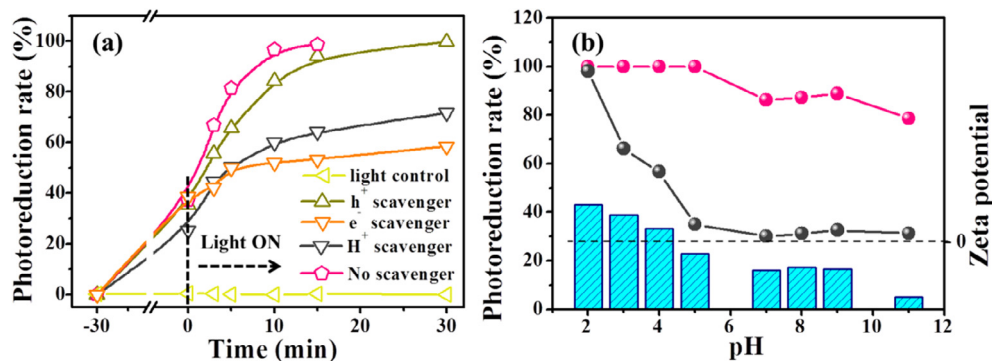


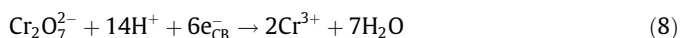
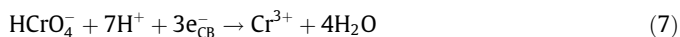
Fig. 9. (a and b) The photocatalytic reduction rate of Cr(VI) versus the irradiation time over different catalysts under visible light irradiation.



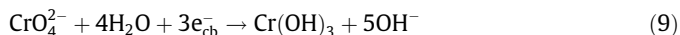
**Fig. 10.** (a) Variation on the photoreduction rate of Cr(VI) with the addition of scavengers; (b) photoreduction rate (pink curve), adsorption rate (black curve) and zeta potential (histogram) of S1 at different pH values (from 2 to 11). (For interpretation of the references to colour in this figure legend, the reader is referred to the web version of this article.)

charged and vice versa, due to the influences of pH on the isoelectric point and redox pathway of catalyst. When the pH value of  $K_2Cr_2O_7$  solution was between 1 and 7,  $HCrO_4^-$  and  $Cr_2O_7^{2-}$  ions were the prevailing Cr(VI) species and gradually deprotonated as pH increased. While at  $pH > 7$ ,  $CrO_4^{2-}$  ions mainly existed in the solution. The redox pathway was given as follows:

In acid medium:



While in neutral or alkaline medium:



Based on the above analysis, when the pH value of the reaction system was below 6, the surface of  $Bi_2S_3$  hierarchitectures (positively charged) was strongly protonated and electrostatically

attracted negatively charged Cr(VI) species (chiefly  $HCrO_4^-$ ), thus promoting the visible-light-driven catalysis. While increasing the pH of the reaction system to alkaline range, the protonated and adsorbed Cr(VI) species on the surface of catalysts decreased, and thus led to relatively low photoreduction ability. Even so,  $Bi_2S_3$  hierarchitectures was still able to remove at least 80% of Cr(VI) within short reaction time (no greater than 30 min) in a wide pH range.

### 3.5. Kinetics and cyclability

To further investigate the effects of Cr(VI) concentration and catalyst dosage on the photoreduction activity of  $Bi_2S_3$  hierarchitectures, a series of kinetic studies were carried out. Fig. 11a depicts the influence of initial Cr(VI) concentration on the photoreduction activity. It was observed that  $Bi_2S_3$  hierarchitectures showed relatively high and steady photoreduction efficiency for Cr(VI) solution with different concentrations (from 40 to

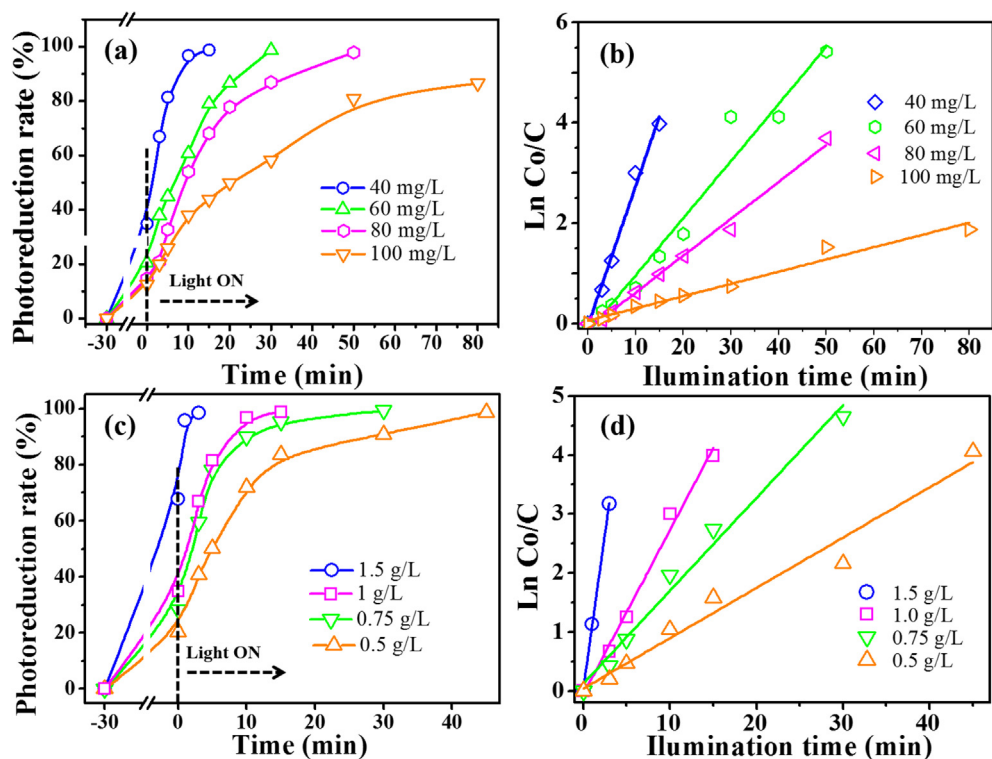


**Fig. 11.** (a) photocatalytic reduction of Cr(VI) with different concentrations of initial Cr(VI) solution and (b) the corresponding kinetics of photoreduction process, (c) photocatalytic reduction of Cr(VI) with different catalyst dosage and (d) the corresponding kinetics of photoreduction process.

100 mg/L). With increase of Cr(VI) concentration, it is necessary to increase the irradiation time to completely remove Cr(VI). Only 87% photoreduction rate was achieved even if the irradiation time was increased to 80 min when the initial Cr(VI) concentration was 100 mg/L.

To quantitatively understand the reaction kinetics of Cr(VI) photoreduction in the present photocatalysis system, the pseudo-first-order model  $\ln(C_0/C) = kt$  was used to express the photoreduction process, where  $C$  is the concentration of Cr(VI) in solution at time  $t$ ,  $C_0$  is the initial Cr(VI) concentration, and  $k$  ( $\text{min}^{-1}$ ) is the apparent pseudo first-order rate constant. Fig. 11b shows the plot of  $\ln(C_0/C)$  versus irradiation time for the Cr(VI) photoreduction process of  $\text{Bi}_2\text{S}_3$  hierarchitectures. The determined reaction rates constant  $k$  and determination coefficient ( $R^2$ ) were summarized in Table 3.

The influence of catalyst dosage on the photoreduction process was also carried out by varying the concentration of  $\text{Bi}_2\text{S}_3$  catalysts in the photocatalysis system. As shown in Fig. 11c and d, both of the photoreduction activity and the pseudo-first-order rate con-

**Table 3**

The pseudo first-order rate constant ( $k$ ) and determination coefficient of photocatalytic reaction over  $\text{Bi}_2\text{S}_3$  hierarchitectures (**S1**) with different concentrations of initial Cr(VI) solutions and catalysts.

Catalyst concentration (g/L)	Initial Cr(VI) concentration (mg/L)	$k$ ( $\text{min}^{-1}$ )	$R^2$
1	40	0.278	0.9862
1	60	0.113	0.9614
1	80	0.073	0.9914
1	100	0.024	0.9702
0.5	40	0.0749	0.9222
0.75	40	0.1573	0.9818
1.5	40	1.052	0.99858

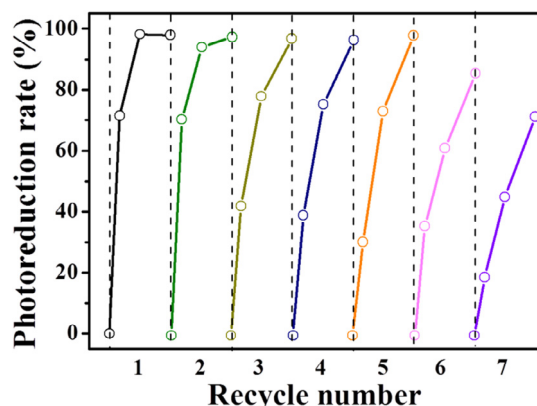


**Fig. 12.** Recycling performance of  $\text{Bi}_2\text{S}_3$  hierarchitectures (**S1**) for photoreduction of Cr(VI).

**Table 4**

Metal ions and organics content in electroplating and tannery wastewater.

Electroplating Wastewater			Tannery Wastewater		
Ion	Concentration (mg/L)		Ion & Organic	Concentration (mg/L)	
	Minimum	Maximum		Minimum	Maximum
$\text{Cu}^{2+}$	0.5	4.5	$\text{Cl}^-$	1000	1500
$\text{Cd}^{2+}$	0.5	1	$\text{SO}_4^{2-}$	1000	2000
$\text{Ni}^{2+}$	0.2	2	$\text{NH}_3$	30	90
$\text{Zn}^{2+}$	1	4	Phenol	5	10

stant was boosted with increase of  $\text{Bi}_2\text{S}_3$  dosage, being ascribed to the increase of Cr(VI) adsorption amounts and surface reaction sites.

The repeatability and stability of  $\text{Bi}_2\text{S}_3$  hierarchitectures (**S1**) were examined. These experiments were performed in a way that the Cr(VI) solution was irradiated for 30 min after 30 min seeking time, in which the photocatalyst was then recollected and washed with 1 mol/L  $\text{HNO}_3$  aqueous solution in each recycle run to remove superficial  $\text{Cr}(\text{OH})_3$  on the catalyst surface. As shown in Fig. 12, after 5 photoreduction cycles of Cr(VI) solution, the photoreduction rate of Cr(VI) still maintained at 97%, indicating that the as-synthesized  $\text{Bi}_2\text{S}_3$  hierarchitectures possess good recyclability and show potential for industrial applications.

Generally, electroplating and tannery wastewater are the most common Cr(VI)-containing wastewater in industry. The main coexisting species (i.e. ions and organics) and the corresponding concentration range in these two kinds of wastewater were listed in Table 4. In order to develop the practical application of hierarchical  $\text{Bi}_2\text{S}_3$  nanospheres in Cr(VI) wastewater treatment, the effect of various parameters, including interfering ions, organics, dissolved gas and temperature on Cr(VI) photoreduction were examined.

Firstly, the Cr(VI) photoreduction efficiency of hierarchical  $\text{Bi}_2\text{S}_3$  nanospheres (**S1**) in the presence of interfering ions  $\text{Cu}^{2+}$ ,  $\text{Cd}^{2+}$ ,  $\text{Ni}^{2+}$  and  $\text{Zn}^{2+}$  with various concentration were examined, respectively. As shown in Fig. 13a–d, the presence of  $\text{Cu}^{2+}$ ,  $\text{Cd}^{2+}$ ,  $\text{Ni}^{2+}$  and  $\text{Zn}^{2+}$  with various concentrations showed no obvious influence on the Cr(VI) photoreduction. On the other hand, an enhancement of Cr(VI) photoreduction activity could be easily found when introducing  $\text{Cl}^-$  or  $\text{SO}_4^{2-}$  into the reaction system, (Fig. Fig. 13e–f). It is probably due to the fact that  $\text{Cl}^-$  or  $\text{SO}_4^{2-}$  could act as electron shuffles and facilitate electron transfer in the reaction solution, which accelerate the process of Cr(VI) reduction by photogenerated electrons [48]. In addition, two non-ionic disruptive substances were added to the photocatalysis system to test the Cr(VI) photoreduction efficiency of hierarchical  $\text{Bi}_2\text{S}_3$  microspheres. As shown in Fig. 13g and h, different concentrations of  $\text{NH}_3$  and phenol has no obvious effect on the performance of Cr(VI) photoreduction by as-prepared  $\text{Bi}_2\text{S}_3$  microspheres.

Fig. 14a illustrated the effect of dissolved gas ( $\text{N}_2$  and  $\text{O}_2$ ) on the photocatalytic efficiency of  $\text{Bi}_2\text{S}_3$  hierarchical microspheres (**S1**), which indicated that the Cr(VI) photoreduction efficiency was slightly influenced by the nature of the dissolved gas. **S1** exhibited lower Cr(VI) photoreduction efficiency in the presence of  $\text{O}_2$ , because oxygen could compete with Cr(VI) for photogenerated electrons, as an electron acceptor. When  $\text{O}_2$  was eliminated by  $\text{N}_2$ , the photoreduction efficiency was improved because more electrons transferred from the surface of **S1** sample to Cr(VI). Fig. 14b elucidated the temperature effect on Cr(VI) photoreduction process. It was found that the high temperature could promote the Cr(VI) photoreduction efficiency, indicating that high temperature had positive influence on the Cr(VI) photoreduction process. High temperature also accelerated the photoreduction of Cr(VI)

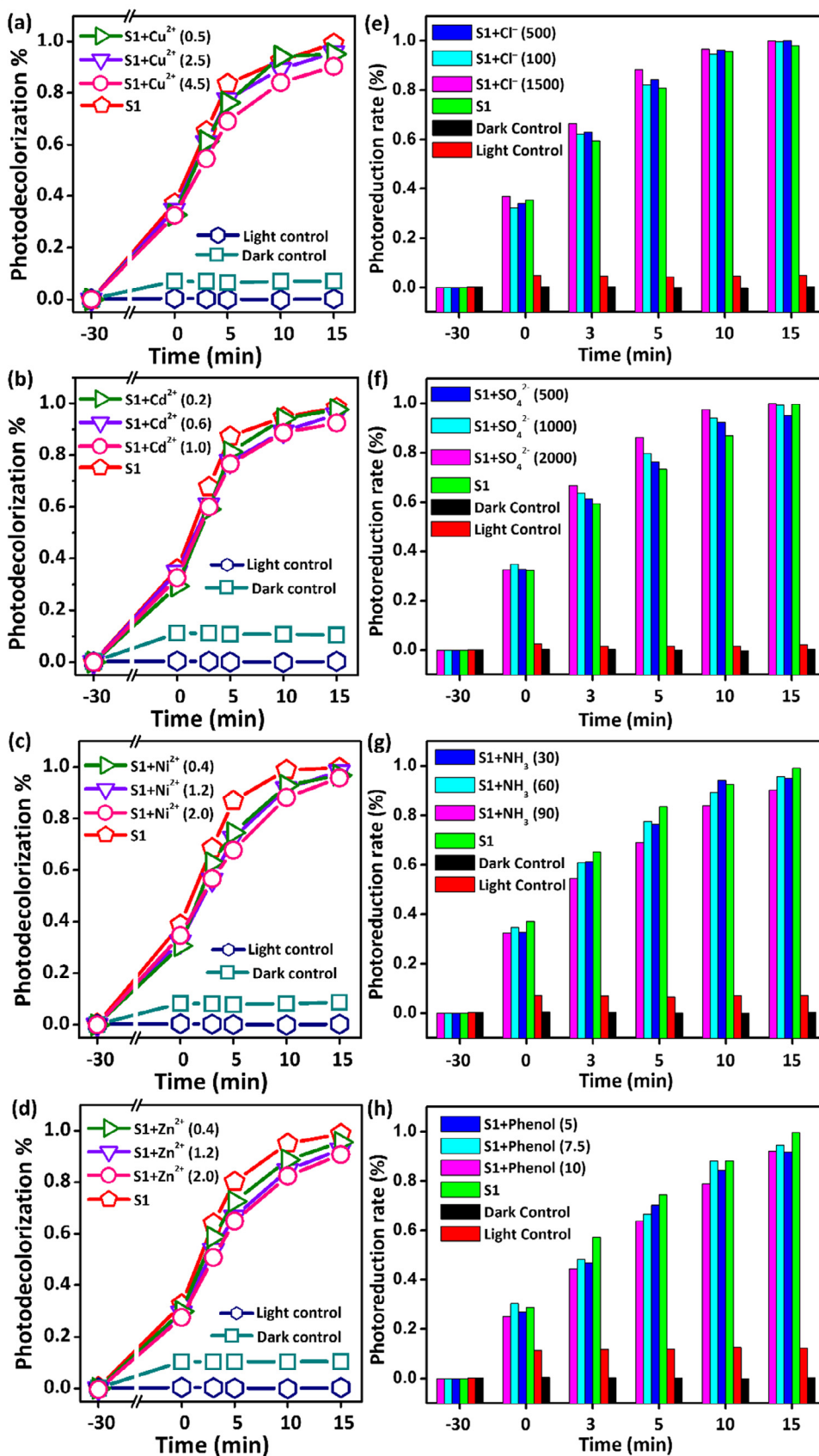


Fig. 13. Effects of interfering ions Cu<sup>2+</sup> (a), Cd<sup>2+</sup> (b), Ni<sup>2+</sup> (c), Zn<sup>2+</sup> (d), Cl<sup>-</sup> (e), SO<sub>4</sub><sup>2-</sup> (f) and disruptive substance NH<sub>3</sub> (g) and Phenol (h) with different concentration on Cr(VI) photoreduction efficiency of S1 sample.

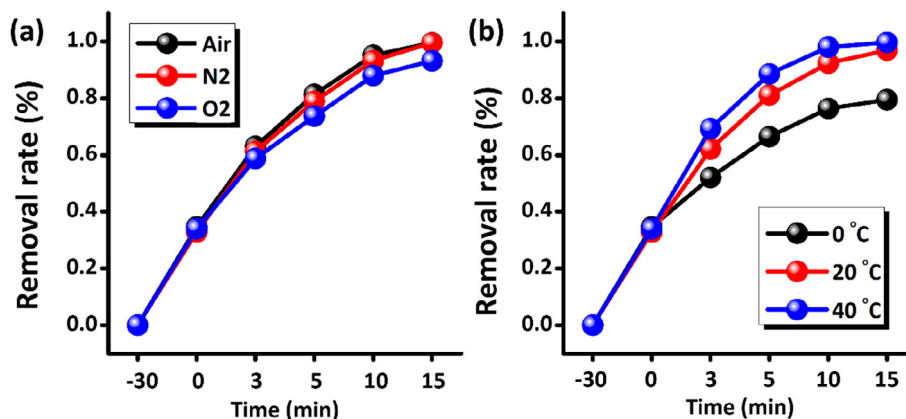


Fig. 14. Effects of dissolved gas (a) and temperature (b) on Cr(VI) photoreduction over S1 sample.

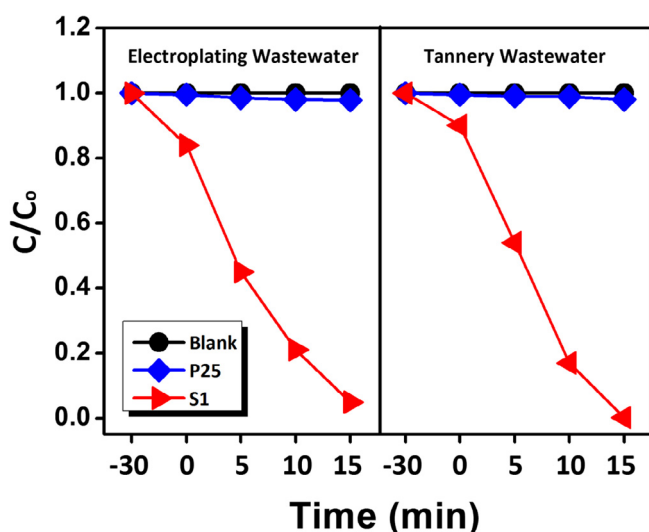


Fig. 15. Cr(VI) photoreduction efficiency of hierarchical Bi<sub>2</sub>S<sub>3</sub> nanospheres (S1) in actual electroplating and tannery industry wastewater.

due to the enhancement of chromium and photogenerated electrons diffusion at high temperature.

To evaluate the practical Cr(VI) photoreduction ability of the as-synthesized Bi<sub>2</sub>S<sub>3</sub> hierarchical nanospheres (S1) in real industrial wastewater, electroplating and tannery wastewater were selected as target pollutants to perform the Cr(VI) photoreduction experiments. As shown in Fig. 15, Cr(VI) was completely reduced both in the electroplating and tannery wastewater within 15 min in the presence of S1 sample under visible light irradiation, while only negligible Cr(VI) was removed over commercial P25. The excellent photoreductive ability and fast photoreduction rate was ascribed to the remarkable photoreduction ability of hierarchical Bi<sub>2</sub>S<sub>3</sub> nanospheres, which implied that it was of great potential in actual wastewater treatment.

#### 4. Conclusion

In summary, Bi<sub>2</sub>E<sub>3</sub> (E = S, Se, and Te) hierarchitectures have been successfully synthesized by an ionic-assisted and microwave-ultrasonic combined irradiation route. Phase transformation and structure evolution of Bi<sub>2</sub>S<sub>3</sub> hierarchitectures from BiOCl microsphere were investigated by XRD, Raman, XPS, SEM, and TEM in detail. The structure, size and morphology tailoring of Bi<sub>2</sub>S<sub>3</sub> hierarchitectures has been achieved by varying the chlorination time,

the alkyl chain length, and concentration of ionic liquid. Photocatalysis study showed that pH value of reaction system, Cr(VI) concentration, and catalyst dosage have a significant influence on the Cr(VI) photoreduction capacity of Bi<sub>2</sub>S<sub>3</sub> hierarchitectures. Compared with P25, BiOCl, and irregular Bi<sub>2</sub>S<sub>3</sub> nanostructures, the as-synthesized Bi<sub>2</sub>S<sub>3</sub> hierarchitectures exhibited superior capacity for photoreduction of Cr(VI), which was strongly attributed to the intrinsic good electron transfer ability, the high surface areas to adsorb more dye molecules and superior light scattering ability of hierarchitectures to enhance the light harvesting efficiency and promote charge transfer ability. It is expected that the as-prepared Bi<sub>2</sub>S<sub>3</sub> hierarchitectures could be used as a potential photocatalyst for the reduction of Cr(VI) based on its good photocatalytic activity and recyclability. More importantly, the Bi<sub>2</sub>S<sub>3</sub> hierarchical nanostructures showed excellent Cr(VI) photoreduction ability and fast photoreduction rate for actual electroplating and tannery industry wastewater treatment. This work will demonstrate further exploration of hierarchical nanostructures with high potential for hazardous Cr(VI) photoreduction in wastewater.

#### Acknowledgements

This work was supported by National Natural Science Foundation of China (21471121 and 21671153), Department of Education of Hubei Province under the project of Science and Technology Innovation Team of Outstanding Young and Middle-aged Scientists (T201606) and Open Project of State Key Laboratory of Inorganic Synthesis and Preparative Chemistry (2017-02).

#### Appendix A. Supplementary data

Supplementary data associated with this article can be found, in the online version, at <http://dx.doi.org/10.1016/j.cej.2017.06.119>.

#### References

- [1] M. Hartmann, A.G. Machoke, W. Schwieger, Catalytic test reactions for the evaluation of hierarchical zeolites, *Chem. Soc. Rev.* 45 (2016) 3313–3330.
- [2] J. Xiong, G. Cheng, Z. Lu, J. Tang, X. Yu, R. Chen, BiOCl hierarchical nanostructures: shape-controlled solvothermal synthesis and photocatalytic degradation performances, *CrystEngComm* 13 (2011) 2381–2390.
- [3] J. Xiong, G. Cheng, G. Li, F. Qin, R. Chen, Well-crystallized square-like 2D BiOCl nanoplates: mannitol-assisted hydrothermal synthesis and improved visible-light-driven photocatalytic performance, *RSC Adv* 1 (2011) 1542–1553.
- [4] J. Tang, H. Zhao, G. Li, Z. Lu, S. Xiao, R. Chen, Citrate/urea/solvent mediated self-assembly of (BiO)<sub>2</sub>CO<sub>3</sub> hierarchical nanostructures and their associated photocatalytic performance, *Ind. Eng. Chem. Res.* 52 (2013) 12604–12612.
- [5] Z. Dai, F. Qin, H. Zhao, F. Tian, Y. Liu, R. Chen, Time-dependent evolution of the Bi<sub>3.64</sub>Mo<sub>0.36</sub>O<sub>6.55</sub>/Bi<sub>2</sub>MoO<sub>6</sub> heterostructure for enhanced photocatalytic activity via the interfacial hole migration, *Nanoscale* 7 (2015) 11991–11999.

- [6] J. Xiong, G. Cheng, F. Qin, R. Wang, H. Sun, R. Chen, Tunable BiOCl hierarchical nanostructures for high-efficient photocatalysis under visible light irradiation, *Chem. Eng. J.* 220 (2013) 228–236.
- [7] J. Jiang, K. Zhao, X. Xiao, L. Zhang, Synthesis and facet-dependent photoreactivity of BiOCl single-crystalline nanosheets, *J. Am. Chem. Soc.* 134 (2012) 4473–4476.
- [8] Q. Deng, X. Duan, D.H.L. Ng, H. Tang, Y. Yang, M. Kong, Z. Wu, W. Cai, G. Wang, Ag nanoparticle decorated nanoporous ZnO microrods and their enhanced photocatalytic activities, *ACS Appl. Mater. Interfaces* 4 (2012) 6030–6037.
- [9] Q. Zhang, Q. Zhang, H. Wang, Y. Li, A high efficiency microreactor with Pt/ZnO nanorod arrays on the inner wall for photodegradation of phenol, *J. Hazard. Mater.* 254 (2013) 318–324.
- [10] Q. Wang, B. Geng, S. Wang, ZnO/Au hybrid nanoarchitectures: wet-chemical synthesis and structurally enhanced photocatalytic performance, *Environ. Sci. Technol.* 43 (2009) 8968–8973.
- [11] H. Cheng, B. Huang, X. Qin, X. Zhang, Y. Dai, A controlled anion exchange strategy to synthesize Bi<sub>2</sub>S<sub>3</sub> nanocrystals/BiOCl hybrid architectures with efficient visible light photoactivity, *Chem. Commun.* 48 (2012) 97–99.
- [12] A.M. Ganose, C.N. Savory, D.O. Scanlon, Beyond methylammonium lead iodide: prospects for the emergent field of ns<sup>2</sup> containing solar absorbers, *Chem. Commun.* 53 (2017) 20–44.
- [13] B. Li, Y. Zhang, R. Du, L. Gan, X. Yu, Synthesis of Bi<sub>2</sub>S<sub>3</sub>-Au dumbbell heteronanostructures with enhanced photocatalytic and photoresponse properties, *Langmuir* 32 (2016) 11639–11645.
- [14] S. Balachandran, M. Swaminathan, The simple, template free synthesis of a Bi<sub>2</sub>S<sub>3</sub>-ZnO heterostructure and its superior photocatalytic activity under UV-A light, *Dalton Trans.* 42 (2013) 5338–5347.
- [15] F. Dong, X. Feng, Y. Zhang, C. Gao, Z. Wu, An anion-exchange strategy for 3D hierarchical (BiO)<sub>2</sub>CO<sub>3</sub>/amorphous Bi<sub>2</sub>S<sub>3</sub> heterostructures with increased solar absorption and enhanced visible light photocatalysis, *RSC Adv.* 5 (2015) 11714–11723.
- [16] Z. Zhang, W. Wang, L. Wang, S. Sun, Enhancement of visible-light photocatalysis by coupling with narrow-band-gap semiconductor: A case study on Bi<sub>2</sub>S<sub>3</sub>/Bi<sub>2</sub>WO<sub>6</sub>, *ACS Appl. Mater. Interfaces* 4 (2012) 593–597.
- [17] B. Weng, X. Zhang, N. Zhang, Z. Tang, Y. Xu, Two-dimensional MoS<sub>2</sub> nanosheet-coated Bi<sub>2</sub>S<sub>3</sub> discs: synthesis, formation mechanism, and photocatalytic application, *Langmuir* 31 (2015) 4314–4322.
- [18] L. Chen, J. He, Q. Yuan, Y. Liu, C. Au, S. Yin, Environmentally benign synthesis of branched Bi<sub>2</sub>O<sub>3</sub>-Bi<sub>2</sub>S<sub>3</sub> photocatalysts by an etching and re-growth method, *J. Mater. Chem. A* 3 (2015) 1096–1102.
- [19] H. He, S.P. Berglund, P. Xiao, W.D. Chemelewski, Y. Zhang, C.B. Mullins, Nanostructured Bi<sub>2</sub>S<sub>3</sub>/WO<sub>3</sub> heterojunction films exhibiting enhanced photoelectrochemical performance, *J. Mater. Chem. A* 1 (2013) 12826–12834.
- [20] D. Ma, M. Guan, S. Liu, Y. Zhang, C. Zhang, Y. He, S.-M. Huang, Controlled synthesis of olive-shaped Bi<sub>2</sub>S<sub>3</sub>/BiVO<sub>4</sub> microspheres through a limited chemical conversion route and enhanced visible-light-responding photocatalytic activity, *Dalton Trans.* 41 (2012) 5581–5586.
- [21] X. Gao, H.B. Wu, L. Zheng, Y. Zhong, Y. Hu, X.W. Lou, Formation of mesoporous heterostructured BiVO<sub>4</sub>/Bi<sub>2</sub>S<sub>3</sub> hollow discs with enhanced photoactivity, *Angew. Chem. Int. Ed.* 53 (2014) 5917–5921.
- [22] D. Li, L. Hu, Y. Xie, G. Niu, T. Liu, Y. Zhou, L. Gao, B. Yang, J. Tang, Low-temperature-processed amorphous Bi<sub>2</sub>S<sub>3</sub> film as an inorganic electron transport layer for perovskite, *ACS Photonics* 3 (2016) 2122–2128.
- [23] Y. Huang, W. Fan, B. Long, H. Li, F. Zhao, Z. Liu, Y. Tong, H. Ji, Visible light Bi<sub>2</sub>S<sub>3</sub>/Bi<sub>2</sub>O<sub>3</sub>/Bi<sub>2</sub>O<sub>2</sub>CO<sub>3</sub> photocatalyst for effective degradation of organic pollutants, *Appl. Catal. B* 185 (2016) 68–76.
- [24] J. Wu, F. Qin, G. Cheng, H. Li, Y. Xie, H. Yang, Z. Lu, X. Yu, R. Chen, Large-scale synthesis of bismuth sulfide nanorods by microwave irradiation, *J. Alloys Compd.* 509 (2011) 2116–2126.
- [25] L. Li, R. Cao, Z. Wang, J. Li, L. Qi, Template synthesis of hierarchical Bi<sub>2</sub>E<sub>3</sub> (E = S, Se, Te) core-shell microspheres and their electrochemical and photoresponsive properties, *J. Phys. Chem. C* 113 (2009) 18075–18081.
- [26] L. Li, N. Sun, Y. Huang, Y. Qin, N. Zhao, J. Gao, M. Li, H. Zhou, L. Qi, Topotactic transformation of single-crystalline precursor discs into disc-like Bi<sub>2</sub>S<sub>3</sub> nanorod networks, *Adv. Funct. Mater.* 18 (2008) 1194–1201.
- [27] J. Jiang, S. Yu, W. Yao, H. Ge, G. Zhang, Morphogenesis and crystallization of Bi<sub>2</sub>S<sub>3</sub> nanostructures by an ionic liquid-assisted templating route: Synthesis, formation mechanism, and properties, *Chem. Mater.* 17 (2005) 6094–6100.
- [28] M. Baghbanzadeh, L. Carbone, P.D. Cozzoli, C.O. Kappe, Microwave-assisted synthesis of colloidal inorganic nanocrystals, *Angew. Chem. Int. Ed.* 50 (2011) 11312–11359.
- [29] H. Xu, B.W. Zeiger, K.S. Suslick, Sonochemical synthesis of nanomaterials, *Chem. Soc. Rev.* 42 (2013) 2555–2567.
- [30] X. Yujiang, C. Huaqiang, L. Kaiyu, Z. Sichun, C. Victoria, The synthesis of superhydrophobic Bi<sub>2</sub>S<sub>3</sub> complex nanostructures, *Nanotechnology* 21 (2010) 145601.
- [31] S. Wang, Y. Du, Preparation of nanocrystalline bismuth sulfide thin films by asynchronous-pulse ultrasonic spray pyrolysis technique, *J. Cryst. Growth* 236 (2002) 627–634.
- [32] G. Cheng, J. Xiong, F.J. Stadler, Facile template-free and fast refluxing synthesis of 3D desertrose-like BiOCl nanoarchitectures with superior photocatalytic activity, *New J. Chem.* 37 (2013) 3207–3213.
- [33] R. Chen, M.H. So, J. Yang, F. Deng, C. Che, H. Sun, Fabrication of bismuth subcarbonate nanotube arrays from bismuth citrate, *Chem. Commun.* (2006) 2265–2267.
- [34] R. Chen, G. Cheng, M.H. So, J. Wu, Z. Lu, C. Che, H. Sun, Bismuth subcarbonate nanoparticles fabricated by water-in-oil microemulsion-assisted hydrothermal process exhibit anti-*Helicobacter pylori* properties, *Mater. Res. Bull.* 45 (2010) 654–658.
- [35] J. Ma, X. Liu, J. Lian, X. Duan, W. Zheng, Ionothermal synthesis of BiOCl nanostructures via a long-chain ionic liquid precursor route, *Cryst. Growth Des.* 10 (2010) 2522–2527.
- [36] C.F. Guo, S. Cao, J. Zhang, H. Tang, S. Guo, Y. Tian, Q. Liu, Topotactic transformations of superstructures: from thin films to two-dimensional networks to nested two-dimensional networks, *J. Am. Chem. Soc.* 133 (2011) 8211–8215.
- [37] Z.A. Peng, X. Peng, Nearly monodisperse and shape-controlled CdSe nanocrystals via alternative routes: nucleation and growth, *J. Am. Chem. Soc.* 124 (2002) 3343–3353.
- [38] B. Pejova, I. Grozdanov, Structural and optical properties of chemically deposited thin films of quantum-sized bismuth (III) sulfide, *Mater. Chem. Phys.* 99 (2006) 39–49.
- [39] H. Liu, Q. Liu, X. Zhao, Crystal growth and optical properties of CdS-doped lead silicate glass, *Mater. Charact.* 58 (2007) 96–100.
- [40] S. Balachandran, N. Prakash, K. Thirumalai, M. Muruganandham, M. Sillanpää, M. Swaminathan, Facile construction of heterostructured BiVO<sub>4</sub>-ZnO and its dual application of greater solar photocatalytic activity and self-cleaning property, *Ind. Eng. Chem. Res.* 53 (2014) 8346–8356.
- [41] B. He, B. Dong, H. Li, Preparation and electrochemical properties of Ag-modified TiO<sub>2</sub> nanotube anode material for lithium-ion battery, *Electrochem. Commun.* 9 (2007) 425–430.
- [42] T. Zhai, L. Li, Y. Ma, M. Liao, X. Wang, X. Fang, J. Yao, Y. Bando, D. Golberg, One-dimensional inorganic nanostructures: synthesis, field-emission and photodetection, *Chem. Soc. Rev.* 40 (2011) 2986–3004.
- [43] H. Liang, S. Liu, S. Yu, Controlled synthesis of one-dimensional inorganic nanostructures using pre-existing one-dimensional nanostructures as templates, *Adv. Mater.* 22 (2010) 3925–3937.
- [44] F.M. Capece, V.D. Castro, C. Furlani, G. Mattogno, C. Fragale, M. Gargano, M. Rossi, “Copper chromite” catalysts: XPS structure elucidation and correlation with catalytic activity, *J. Electron. Spectrosc.* 27 (1982) 119–128.
- [45] E. Desimoni, C. Malitesta, P.G. Zamboni, J.C. Rivière, An x-ray photoelectron spectroscopic study of some chromium-oxygen systems, *Surf. Interface Anal.* 13 (1988) 173–179.
- [46] Z. Fang, Y. Liu, Y. Fan, Y. Ni, X. Wei, K. Tang, J. Shen, Y. Chen, Epitaxial growth of CdS nanoparticle on Bi<sub>2</sub>S<sub>3</sub> nanowire and photocatalytic application of the heterostructure, *J. Phys. Chem. C* 115 (2011) 13968–13976.
- [47] H.T. Shaban, M.M. Nassary, M.S. El-Sadek, Transport properties of Bi<sub>2</sub>S<sub>3</sub> single crystals, *Phys. B* 403 (2008) 1655–1659.
- [48] G. Li, X. Liu, H. Zhang, P. Wong, T. An, H. Zhao, Comparative studies of photocatalytic and photoelectrocatalytic inactivation of *E. coli* in presence of halides, *Appl. Catal. B* 140–141 (2013) 225–232.